Title

A novel constitutive model for passive right ventricular myocardium: evidence for myofiber–collagen fiber mechanical coupling

Journal

Biomechanics and Modeling in Mechanobiology, 16(2)

ISSN

1617-7959

Authors

Avazmohammadi, Reza
Hill, Michael R
Simon, Marc A
et al.

Publication Date

2017-04-01

DOI

10.1007/s10237-016-0837-7

Peer reviewed

HHS Public Access

Author manuscript

Biomech Model Mechanobiol. Author manuscript; available in PMC 2018 April 01.

Published in final edited form as:

Biomech Model Mechanobiol. 2017 April ; 16(2): 561–581. doi:10.1007/s10237-016-0837-7.

A novel constitutive model for passive right ventricular myocardium: Evidence for myofiber-collagen fiber mechanical coupling

Reza Avazmohammadi[1], **Michael Hill**[2], **Marc Simon**[3], **Will Zhang**[1], and **Michael Sacks**[1]

[1]*Center for Cardiovascular Simulation*, Institute for Computational Engineering and Sciences and the Department of Biomedical Engineering, The University of Texas at Austin

[2]School of Mathematical Sciences, the University of Nottingham

[3]Departments of Cardiology and Bioengineering, Heart and Vascular Institute, The University of Pittsburgh

Abstract

The function of right ventricle (RV) is recognized to play a key role in the development of many cardiopulmonary disorders, such as pulmonary arterial hypertension (PAH). Given the strong link between tissue structure and mechanical behavior, there remains a need for a myocardial constitutive model that accurately accounts for right ventricular myocardium architecture. Moreover, most available myocardial constitutive models approach myocardium at the length scale of mean fiber orientation, and do not explicitly account for different fibrous constituents and possible interactions among them. In the present work, we developed a fiber-level constitutive model for the passive mechanical behavior of the right ventricular free wall (RVFW) that explicitly distinguished between the mechanical contributions of myofiber and collagen fiber ensembles, and accounted for the fiber mechanical interactions. To obtain model parameters for the healthy passive RVFW, the model was informed by transmural orientation distribution measurements of myo- and collagen fibers, and was fit to the mechanical testing data, where both sets of data were obtained from recent experimental studies on non-contractile, but viable, murine RVFW specimens. Results supported the hypothesis that in the low strain regime the behavior of the RVFW is governed by myofiber response alone, which does not demonstrate any coupling between different myofiber ensembles. At higher strains, the collagen fibers and their interactions with myofibers begin to gradually contribute and dominate the behavior as recruitment proceeds. Due to the use of viable myocardial tissue, the contribution of myofibers was significant at all strains with the predicted tensile modulus of ~ 35 kPa. This was in contrast to earlier reports (Horowitz et al. 1988) where the contribution of myofibers was found to be insignificant. Also, we found that the interaction between myo- and collagen fibers was greatest under equibiaxial strain, with its contribution to the total stress not exceeding 20%. The present model can be applied to organlevel computational models of right ventricular dysfunction for efficient diagnosis and evaluation of pulmonary hypertension disorder.

For correspondence: Michael S. Sacks, Ph.D., W. A. Moncrief, Jr. Simulation-Based Engineering Science Chair I, Institute for Computational Engineering and Sciences, Department of Biomedical Engineering, The University of Texas at Austin, 201 East 24th Street, ACES 5.438, 1 University Station, C0200, Austin TX 78712-0027 U.S.A., msacks@ices.utexas.edu, Tel: 512-232-7773.

1 Introduction

The right ventricle of the heart is recognized to play a vital role in cardiopulmonary disorders such as pulmonary arterial hypertension, myocardial ischemia, and congestive heart failure. In particular, 70% of patients suffering from pulmonary arterial hypertension (PAH) will ultimately succumb to right ventricular (RV) failure (Voelkel et al. 2011). The health and status of the right ventricle of the heart has been shown to be a key indicator of overall progression of PAH (Stone and Klinger 2008) and, thus, a good predictor of survival for patients suffering from this disease. From mechanistic point of view, PAH imposes a pressure overload on the RV myocardium, also known as RV free wall (RVFW), leading to elevated transmural wall stress, and subsequently to progressive hypertrophy and remodeling of RV, which ultimately results in mechanical failure of the right heart (Bogaard et al. 2009; Simon 2010). Although significant clinical progress has been made to date in assessing the RV response to hypertension (Champion et al. 2009; Forfia et al. 2008; Hemnes and Champion 2008; Kodama and Takimoto 2000) and in developing new treatments for PAH (Forfia et al. 2006; Forfia et al. 2008; Hemnes and Champion 2008; Kodama and Takimoto 2000; Vigano et al. 2004), there still exists a pressing need to develop computational biomechanical models of the right ventricle that can estimate the onset and progression of RV hypertrophy and the limits of its reversibility, given necessary organ-level clinical measurements.

The development of such models relies, of course, on the development of an appropriate tissue-level constitutive model. The major steps in determining a concise, robust constitutive model for the mechanical behavior of any soft tissue include: (I) developing a consistent mathematical framework, (II) using the model to design the necessary experiments that contain sufficient information to represent the three-dimensional mechanical properties and microstructure of the myocardium, and (III) conducting robust model parameter estimation, and finally (IV) evaluating the predictive capability of the model. Beyond these standard concerns, additional complexities are encountered in modeling myocardium due to its highly heterogeneous, complex 3D structure. Specifically, myocardium consists of myofibers, collagen fibers, a vascular network (approximately 10–20% of its volume), specialized conduction tissues, and an amorphous ground matrix (Fox and Hutchins 1972; Hasenkam et al. 1994). Unlike the left ventricle (LV), histological studies on the RVFW revealed that almost all myofibers were locally oriented in the plane normal to the transmural direction of the tissue, with planar angular distribution changing with the depth (Hill et al. 2014), with large collagen fibers oriented nearly parallel to myofibers in the plane of tissue, interconnected with a network of fine collagen fibers.

Consistent with this microstructure, RVFW passive mechanical behavior revealed strongly anisotropic behavior (Hill et al. 2014; Valdez-Jasso et al. 2012). More importantly, comparisons between the healthy and PAH-induced RVFW specimens revealed that the alterations in mechanical properties of the RVFW under influence of PAH are primarily associated with hypertrophy of myofibers and notable changes in transmural orientation distribution of myo- and collagen fibers. Therefore, a constitutive model that will be able to reliably reproduce the biomechanical response of a healthy RVFW and capture its structural

and biomechanical adaptations, when subjected to a sustained pressure overload, must account for the composition, properties, and transmural architecture of the myo- and collagen fibers.

Although numerous studies have been devoted to constitutive modeling of left ventricular (LV) myocardium (e.g. Holzapfel and Ogden (2009) provides a brief review on existing constitutive models of LV myocardium), there exist few models for the RVFW. Early contributions to constitutive modeling of the RVFW are limited (Sacks and Chuong 1992; Sacks and Chuong 1993). In this early work the RVFW was modeled as a continuous stack of incompressible, transversely isotropic pseudoelastic layers with their preferred direction varying linearly from the endocardial surface to the epicardial surface. More recent studies (Hill et al. 2014; Valdez-Jasso et al. 2012) investigated the biaxial mechanical behavior of non-contractile, but viable, murine RVFW specimens of full thickness, and used a basic 2-D transversely isotropic pseudoelastic model to describe the mechanical data. The mechanical behavior revealed mechanical anisotropy with the apex-to-outflow tract direction being the stiffer direction. In addition, the use of viable tissues revealed a nearly linear stress-strain behavior with high stiffness at the low strain regime which was entirely attributed to the response of the myofibers. This is in contrast to the conclusion drawn in Horowitz et al. (1988) where the mechanical contribution of myofibers were found to be insignificant compared to the that of collagen fibers. This might have been due to insufficient viability in the associated mechanical testing data given in Yin et al. (1987). In any event, subsequent to gross observations of tissue behavior, mesoscale structurally-based constitutive models are needed to precisely determine physical mechanisms that take place at the microstructural level in the tissue and their correlation with the tissue-level response.

Mesoscale constitutive models (Kassab and Sacks 2016; Lanir 1983a; Sacks 2003; Zhang et al. 2016) are based on quantitative descriptors that attempt to account for histological features (typically, in the scale of less than 1 mm) and constituents' mechanical properties to establish a quantitative link between the overall mechanical behavior and the underlying micromechanical mechanisms. This feature is particularly important for interests in developing a physical-based growth and remolding (G&R) model for RVFW response under PAH as it will allow us to separate the relative effects of myofiber hypertrophy from changes in fiber reorganization, in relation to the overall changes of the tissue behavior.

As a first step, the objective in the present work is to develop a mesoscale (i.e. at the level of the constituent fibers) structural constitutive model of the *viable* RVFW that accounts for interactions between fibrous constituents. We utilized the comprehensive biaxial mechanical behavior data and quantitative tissue structural information from murine experimental studies (Hill et al. 2014; Valdez-Jasso et al. 2012) to estimate the parameters in our model. To the best of our knowledge, the present study is the first work to provide and quantify a structural model for viable myocardial tissues that explores the potential for the contribution of mechanical interactions between the two major structural fiber families.

2 Methods

2.1 Mechanical testing and structural quantification

Details of the mechanical tests and histological studies have previously presented (Hill et al. 2014). Briefly, a total of 10 RVFW specimens of male rats were subjected to a multiprotocol biaxial mechanical test that encompassed the estimated physiological strain range (Fig. 1a). For the new structural analyses conducted from similarly prepared specimens but from a separate group of animals (consisting of three specimens), myofibers and collagen fibers of the extracellular matrix (ECM) were assumed to be the dominant mechanical constituents comprising the myocardium. It was found that the myo- and collagen fibers had a nearly planar orientation (Hill et al. 2014). The planar fiber orientation distributions were determined by analyzing histologically stained sections (layers) for three specimens (Fig. 1b), similar to those used previously in our lab (Courtney et al. 2006). A total of 10 sections of ~ 50μm thickness were taken of each specimen, which were stained using Gomori One-Step Trichrome to make the myo- and collagen fibers easily discernable. The sections were then imaged, and the orientation distributions for myo- and collagen fibers were separately quantified using standard gradient methods (Hill et al. 2014). In addition, total myo and collagen fiber content was quantified previously (Hill et al. 2014). From these measurements, the average volume fractions of myofibers, collagen fibers, and amorphous ground matrix were approximately determined as $\phi^{m} = 0.69$, $\phi^{c} = 0.29$, and $\phi^{g} = 0.02$, respectively (Hill et al. 2014; Valdez-Jasso et al. 2012). The resulting mechanical and histological data were then referred to a local Cartesian basis (Figs. 1(a) and (b)).

2.2 Fiber morphology

Based on the above histological observations, we assumed that all fibers lie in $\mathbf{e}_1' - \mathbf{e}_2'$ plane (Fig. 1b.) As the analysis of all histological sections used the same coordinate basis $\{\mathbf{e}_1', \mathbf{e}_2', \mathbf{e}_3'\}$, the transmural orientation distribution of the fibers was represented by a probability density function $\rho(\mathbf{v},z)$ in the referential configuration Ω_0, where $\mathbf{v}$ is a planar unit vector identifying the fiber orientation in the plane of tissue and z denotes the normalized thickness variable along transmural direction $\mathbf{e}_3$ (i.e. normal to the plane of tissue). Without loss of generality, we set z to vary between 0 at endocardium to 100 at epicardium. Next, we defined two unit vectors $\mathbf{n}^{m}$ and $\mathbf{n}^{c}$ to describe the (planar) orientation of myo- and collagen fibers, respectively (Fig. 2)

$$\mathbf{n}^{\mathrm{m}}(\theta^{\mathrm{m}})=\cos(\theta^{\mathrm{m}})\mathbf{e}_1'+\sin(\theta^{\mathrm{m}})\mathbf{e}_2', \quad \mathbf{n}^{\mathrm{c}}(\theta^{\mathrm{c}})=\cos(\theta^{\mathrm{c}})\mathbf{e}_1'+\sin(\theta^{\mathrm{c}})\mathbf{e}_2', \quad (1)$$

with the span $\theta^{m}, \theta^{c} \in (-\pi/2, \pi/2]$. Using these definitions, the transmural orientation distribution function takes the functional form $\rho(\mathbf{v},z) = \pi\,\Gamma(\theta,z)$ that satisfies the following normalization conditions

$$\frac{1}{\mathrm{H}}\int_{-\pi/2}^{\pi/2}\int_{0}^{\mathrm{H}}\Gamma^{\mathrm{m}}(\theta^{\mathrm{m}},\mathrm{z})\mathrm{d}\theta^{\mathrm{m}}\mathrm{dz}=1, \quad \frac{1}{\mathrm{H}}\int_{-\pi/2}^{\pi/2}\int_{0}^{\mathrm{H}}\Gamma^{\mathrm{c}}(\theta^{\mathrm{c}},\mathrm{z})\mathrm{d}\theta^{\mathrm{c}}\mathrm{dz}=1, \quad (2)$$

for myo- and collagen fibers, respectively, where H = 100 denotes the (normalized) tissue thickness. To fit a surface to the 3D data, we used the following modified (shifted and scaled) Beta distribution function,

$$\Gamma(\theta, z)=\frac{(1-d)}{\pi}\frac{u^{\gamma-1}(1-u)^{\gamma-1}}{B(\gamma,\gamma)}+\frac{d}{\pi}, \quad (3)$$

where u = u(z) = [θ − μ(z)] / π + 0.5, B is the Beta function with shape factor γ(z), μ(z) denotes the mean fiber direction, and "d " provides a baseline for the distribution and is fixed in the transmural direction. The shape factor γ(z) is related to the variance, σ^2 (z), of the distribution using

$$\gamma(z)=\frac{1}{2}\left(\frac{1}{4\sigma(z)^2}-1\right). \quad (4)$$

For fitting purposes, the variables μ(z) and σ(z) were approximated using 1D Hermitian and Lagrangian shape functions, respectively. It is useful to note that the distribution function (3) is normalized in the plane of tissue such that it satisfies the condition

$$\int_{-\pi/2}^{\pi/2}\Gamma(\theta, z)d\theta=1, \quad (5)$$

for any value of z between 0 and 100.

2.3 Constitutive model formulation

A structural-based model for the effective (tissue-level) mechanical behavior of the RVFW was developed as follows. We idealize the RV myocardium as primarily composed of two major material phases: a dense fibrous phase and a non-fibrous substance. The fibrous phase is subdivided into two mechanically relevant fiber constituents: myo- and collagen fibers. Here, we make a further distinction between two sub-groups of collagen fibers: the "large" perimysial collagen fibers that were observed to run nearly parallel to myofibers (Fig. 3a), and the "fine" endomysial collagen fiber network that surrounds individual myofibers as well as interconnects extensively with the large collagen fibers (Figs. 3a,b) (Borg and Caulfield 1981; Borg et al. 1983). Also, the non-fibrous phase, referred to as the matrix phase, includes remaining mechanically insignificant substances such as vasculature, neural tissues, myofibroblasts, etc. This phase together with the fluid phase are assumed to be responsible for the incompressibility of the tissue and are combined into one single phase.

Based on these structural idealizations, we first consider a representative tissue element (RTE) of RVFW treated as a 3D continuum. The RTE is assumed to be large enough to represent the properties associated with the myocardial microstructure in an average sense, yet small compared to the characteristic length scale of the RVFW (typical RTE size was

3mm × 3mm × 0.5 mm). Upon application of external loading, a material point **X** in the reference configuration of the RTE moves to a new point **x** = **X**(**x**,t) at time t in the deformed configuration of the RTE. The deformation gradient tensor **F** = Grad**x** serves to characterize the deformation of the material. The tissue-level right Cauchy-Green tensor is defined as **C** = $\mathbf{F}^{\mathrm{T}}\mathbf{F}$, and the tissue-level Green-Lagrange strain tensor is given by **E** = (**C** − **I**) / 2, where **I** is the identity tensor.

Ignoring any time-dependency effects, each constituent phase is assumed to exhibit a *pseudo-hyperelastic* behavior (Fung 1993), so that the effective mechanical behavior of the RVFW in loading can be described by a strain energy function $\Psi(\mathbf{C})$. In this work, we assume the affine kinematics for tissue constituents, i.e. the fibers and matrix phases undergo the same deformation applied to the tissue (Fan and Sacks 2014; Lanir 1983b; Lee et al. 2015). The total energy function can be written as the sum of the mechanical contribution of the ground matrix and embedded fibers, as

$$\Psi(\mathbf{C})=\phi^{\mathrm{g}}\Psi^{\mathrm{g}}(\mathbf{C})+\phi^{\mathrm{m}}\Psi^{\mathrm{m}}(\mathbf{C})+\phi^{\mathrm{c}}\overline{\Psi}^{\mathrm{c}}(\mathbf{C})=\phi^{\mathrm{g}}\Psi^{\mathrm{g}}(\mathbf{C})+\phi^{\mathrm{m}}\Psi^{\mathrm{m}}(\mathbf{C})+\phi^{\mathrm{c}}\left[\Psi^{\mathrm{c}}(\mathbf{C})+\Psi^{\mathrm{m-c}}(\mathbf{C})\right], \quad (6)$$

where Ψ^{g}, Ψ^{m} and $\bar{\Psi}^{\mathrm{c}}$ are the strain energy functions associated with the ground matrix phase, myofibers, and collagen fibers. The energy term $\bar{\Psi}^{\mathrm{c}}$ has contributions from large (perimysial) collagen fibers and fine (endomysial) collagen fiber network (Fig. 3b). The latter is hypothesized to drive the interaction (coupling) between myofiber and (large) collagen fibers. Therefore, two terms Ψ^{c} and $\Psi^{\mathrm{m\text{-}c}}$ in (6) are designated to capture the mechanical contribution of large collagen fibers and their interaction with myofibers. Note that ϕ^{c} in (6) represents the total volume fraction of both groups of collagen fibers (as we were able to measure in our experimental analysis). The accurate calculation of amount of energy generated in each group of collagen fibers will be still due to the knowledge of sub-fraction of each collagen group which is absorbed in the respective term in the form (6). Such information is not currently available, however the form (6) is still useful to estimate the contribution of each fiber group to the total energy.

At the tissue level, the second Piola-Kirchhoff stress tensor **S** can be described in terms of the energy function $\Psi(\mathbf{C})$, through

$$\mathbf{S}=2\frac{\partial\Psi}{\partial\mathbf{C}}-\mathrm{p}\mathbf{C}^{-1}=\mathbf{S}^{\mathrm{g}}+\mathbf{S}^{\mathrm{m}}+\mathbf{S}^{\mathrm{c}}+\mathbf{S}^{\mathrm{m-c}}, \quad (7)$$

where $\mathbf{S}^{\mathrm{g}} = 2\phi^{\mathrm{g}}\partial\Psi^{\mathrm{g}}(\mathbf{C}) / \partial\mathbf{C} - \mathrm{p}\mathbf{C}^{-1}$, $\mathbf{S}^{\mathrm{m}} = 2\phi^{\mathrm{m}}\,\partial\Psi^{\mathrm{m}}(\mathbf{C}) / \partial\mathbf{C}$, $\mathbf{S}^{\mathrm{i}} = 2\phi^{\mathrm{c}}\,\partial\Psi^{\mathrm{i}}(\mathbf{C}) / \partial\mathbf{C}$ (i=c, m-c), and p is the unknown hydrostatic pressure to enforce $\det(\mathbf{C})= 1$. In the following, we describe the behavior of each constituent phase.

2.3.1 Matrix—For contribution of the ground matrix phase, based on previous studies (Humphrey and Yin 1987; Sacks and Chuong 1993), it suffices to utilize a single isotropic hyperelastic neo-Hookean model with the strain energy function $\Psi^{g} = k^{g} / 2\,(I_1 - 3)$, where $I_1 = \mathrm{trace}(\mathbf{C})$, and $k^{g} > 0$ is the shear modulus of the matrix in the infinitesimal strain regime. Using the definition of the stress in (7), the resulting stress tensor for the non-fibrous ground matrix and fluid phases is given by

$$\mathbf{S}^{g} = \phi^{g} \left(k^{g} \mathbf{I} - p \mathbf{C}^{-1} \right). \quad (8)$$

2.3.2 Myo- and collagen fibers—Following Lanir (1983a), we define a *fiber ensemble* as the collection of local fibers of the same type within the RTE with a common direction. The collective mechanical contribution from the ensemble is represented by its strain energy Ψ_{ens}. Following the affine kinematics assumption, the deformation along (ensemble) fiber directions $\mathbf{n}^{m}$ and $\mathbf{n}^{c}$ can be characterized by kinematical invariants I^{m} and I^{c} defined as

$$I^{m} = \mathbf{n}^{m} \cdot \mathbf{C}\mathbf{n}^{m}, \quad I^{c} = \mathbf{n}^{c} \cdot \mathbf{C}\mathbf{n}^{c}, \quad (9)$$

where we recall that $\mathbf{n}^{m}$ and $\mathbf{n}^{c}$ represent the local orientation of myo- and collagen fibers, respectively (Fig. 2). It is also useful to define the fiber ensemble strains in the directions $\mathbf{n}^{m}$ and $\mathbf{n}^{c}$ given by

$$E^{m} = \mathbf{n}^{m} \cdot \mathbf{E}\mathbf{n}^{m} = (I^{m} - 1)/2, \quad E^{c} = \mathbf{n}^{c} \cdot \mathbf{E}\mathbf{n}^{c} = (I^{c} - 1)/2, \quad (10)$$

respectively.

Assuming that both types of fibers can only withstand tensile loads, the stored energy in myo- and collagen fiber ensembles can be expressed in terms of deformation along the fiber as $\Psi^{m}_{ens}(I^{m})$ and $\Psi^{m}_{ens}(I^{c})$, respectively. As a result, the total energy over all myo- and (large) collagen fiber ensembles with orientation distributions $\Gamma^{m}(\theta^{m}, z)$ and $\Gamma^{c}(\theta^{c}, z)$ in the RTE is respectively given by

$$\Psi^{m} = \frac{1}{H} \int_{0}^{H} \int_{-\pi/2}^{\pi/2} \Gamma^{m}(\theta^{m}, z)\, \Psi^{m}_{ens}(I^{m})\, d\theta^{m} dz, \quad \Psi^{c} = \frac{1}{H} \int_{0}^{H} \int_{-\pi/2}^{\pi/2} \Gamma^{c}(\theta^{c}, z)\, \Psi^{c}_{ens}(I^{c})\, d\theta^{c} dz, \quad (11)$$

As mentioned earlier, the presence of the dense network of fine collagen fibers connecting to myo- and (large) collagen fibers suggests that there could be an interaction between myo- and collagen fiber ensembles. Since *quantified* information on the detailed architecture of fine collagen fiber network in the RVFW is not yet available, this interaction was modeled in a heuristic fashion at the same length scale of myo- and collagen fibers. One approach to account for the coupling between two fiber ensembles (identified by the directions $\mathbf{n}^{m}$ and $\mathbf{n}^{c}$) is to make use of the deformation invariant $I^{mc} = \mathbf{n}^{m} \cdot \mathbf{C}\mathbf{n}^{c}$ (Spencer 1984) (conventionally

denoted by I_8). Sacks et al. (2016) recently demonstrated that the invariant I^{mc} can be divided into two types of interactions: (i) *extensional interactions* stemming from the product of I^m and I^c, and (ii) rotational interaction accounting for the changes in the angle between $\mathbf{n}^m$ and $\mathbf{n}^c$ (which conveniently vanishes under equibiaxial strains). As will be discussed later (Subsection 4.3), a key interaction term required to accurately capture the mechanical behavior of RVFW tissues was of an extensional nature alone. Based on these considerations, we proposed the following form of energy for myo-collagen *inter-fiber ensemble* interactions

$$\Psi^{m-c}=\frac{1}{H}\int_0^H\int_{-\pi/2}^{\pi/2}\int_{\theta^m-\theta_0^c}^{\theta^m+\theta_0^c}\Gamma^m(\theta^m,z)\,\Gamma^c(\theta^c,z)\,\Psi_{ens}^{m-c}(I^m,I^c)\,d\theta^m d\theta^c dz, \tag{12}$$

where $\Psi_{ens}^{m-c}(I^m,I^c)$ denotes the interaction strain energy between two individual fiber ensembles, and $0\le\theta_0^c\le\pi/2$ identifies the span of adjacency around each ensemble of myofibers within which it interacts with neighboring (large) collagen fiber ensembles. Note that, here, based on the near-planar fiber structure of the RVFW we account only for the interaction between ensembles lying in the same plane.

Strain energy form for myofibers: Results from our experimental findings (Hill et al. 2014) suggest that the myofibers are responsible for the low stress response, followed by increasing contributions of the collagen fibers due to their gradual recruitment with strain. In particular, these studies indicate a nearly linear stress-strain behavior (in the $\mathbf{S}-\mathbf{E}$ space) in the low strain regime, where collagen fiber recruitment has not yet occurred. Our pilot studies indicated that the form $\Psi_{ens}^m(I^m)=k_1^m(\sqrt{I^m}-1)^2/2$, with $k_1^m>0$ being the effective myofiber low-strain tensile modulus, can capture the behavior of the tissue in this regime. However, an exponential descriptor provides a better account for the behavior of myofibers for a full range of strain ($E^m < 0.4$) and is consistent with other myofiber models proposed mainly in the context of LV myocardium (Dokos et al. 2002; Holzapfel and Ogden 2009). Also, the myofibers do not support compression and they tend to buckle in compression (Holzapfel and Ogden 2009). These considerations lead us to propose the following energy function for the myofiber contribution

$$\Psi_{ens}^m(I^m)=\begin{cases}\frac{k_1^m}{2k_2^m}\left\{\exp\left[k_2^m\left(\sqrt{I^m}-1\right)^2\right]-1\right\}, & I^m\ge 1,\\ 0, & I^m<1,\end{cases} \tag{13}$$

where $k_2^m>0$ is a dimensionless parameter. As defined in Eq. $(11)_1$, the homogenized energy function of myofibers (Ψ^m) is obtained as the sum of the energy of all myofiber ensembles, weighted by the 3D orientation distribution function $\Gamma^m(\theta^m, z)$. Making use of (7), the resulting expression for the stress tensor associated with myofibers is given by

$$\mathbf{S}^{\mathrm{m}}=\frac{\phi^{\mathrm{m}}\mathrm{k}_1^{\mathrm{m}}}{\mathrm{H}}\int_0^{\mathrm{H}}\int_{-\pi/2}^{\pi/2}\Gamma^{\mathrm{m}}\left(\theta^{\mathrm{m}},\mathrm{z}\right)\frac{\left(\sqrt{\mathrm{I}^{\mathrm{m}}}-1\right)}{\sqrt{\mathrm{I}^{\mathrm{m}}}}\exp\left[\mathrm{k}_2^{\mathrm{m}}\left(\sqrt{\mathrm{I}^{\mathrm{m}}}-1\right)^2\right]\left(\mathbf{n}^{\mathrm{m}}\otimes\mathbf{n}^{\mathrm{m}}\right)\mathrm{d}\theta^{\mathrm{m}}\mathrm{dz}, \tag{14}$$

for $\mathrm{I}^{\mathrm{m}} \geq 1$, and 0 otherwise.

Strain energy form for large collagen fibers population: In this work, we assume a linear force-displacement relation for large (perimysial) collagen fibers when they are fully straightened, based on the study of (Zhang et al. 2015) for the mechanical behavior of collagen fibers. However, the collagen fibers are known to be undulated in the zero-stress state (Kenedi et al. 1965; Lanir 1979; Millington et al. 1971). (Also see Fig. 3 (c).) Support for this finding arise from scanning electron microscopy analysis of fixed myocardium, in which collagen fibers appeared wavy in diastole and taut in systole (Caulfield and Borg 1979). In addition, collagen fibers are known to have negligible bending stiffness, and the load required to straighten the collagen fiber is also considered to be negligible. Hence, a collagen fiber transmit load only if stretched beyond its slack stretch, denoted by $\lambda_{\mathrm{s}} \geq 1$, where the undulation has disappeared. Based on these considerations, we hypothesize the following energy function for a single collagen fiber

$$\Psi_{\mathrm{fiber}}^{\mathrm{c}}\left(\mathrm{I}^{\mathrm{c}}\right)=\begin{cases}\frac{1}{2}\mathrm{k}^{\mathrm{c}}\left(\sqrt{\mathrm{I}^{\mathrm{c}}}/\lambda_{\mathrm{s}}-1\right)^2 & \mathrm{I}^{\mathrm{c}}\geq\lambda_{\mathrm{s}}^2\\ 0 & \mathrm{I}^{\mathrm{c}}<\lambda_{\mathrm{s}}^2\end{cases}, \tag{15}$$

where k^{c} denotes the (tensile) modulus of a straight collagen fiber. Note that the above form satisfies the conditions of zero energy and zero stress at the threshold of recruitment, i.e. when $\mathrm{I}^{\mathrm{c}}=\lambda_{\mathrm{s}}^2$.

It is known that the degree of fiber undulation can vary considerably among individual collagen fibers (Lanir 1983a). To stochastically account for this variance in the level of fiber ensemble, we define the distribution function $\mathrm{D}(\lambda_{\mathrm{s}})$ over the slack stretch range $\lambda_{\mathrm{s}} \in [\lambda_{\mathrm{lb}}, \lambda_{\mathrm{ub}}]$, where λ_{lb} and λ_{ub} denote the lower and upper bounds of collagen fiber slack stretch within an ensemble, with $\lambda_{\mathrm{ub}} > \lambda_{\mathrm{lb}} > 1$ and $\int_{\lambda_{\mathrm{lb}}}^{\lambda_{\mathrm{ub}}}\mathrm{D}(\lambda_{\mathrm{s}})\mathrm{d}\lambda_{\mathrm{s}}=1$. In this generalized case, the undulation of fibers gradually disappears when I^{c} increases from λ_{lb}^2, and all fibers within the ensemble are recruited at $\mathrm{I}^{\mathrm{c}}=\lambda_{\mathrm{ub}}^2$. The energy form (15) can be accordingly generalized to account for a distribution of slack stretch within an ensemble of collagen fibers. It can be shown that (Fan and Sacks 2014; Lanir 1983a; Lanir 1994; Sacks et al. 2016; Zhang et al. 2015) the generalized form of the ensemble strain energy (which is the sum of individual undulated fiber energies weighted by the distribution $\mathrm{D}(\lambda_{\mathrm{s}})$) is given by

$$\Psi_{\mathrm{ens}}^{\mathrm{c}}\left(\mathrm{I}^{\mathrm{c}}\right)\int_{\lambda_{\mathrm{lb}}}^{\lambda_{\mathrm{ub}}}\mathrm{D}(\lambda_{\mathrm{s}})\Psi_{\mathrm{fiber}}^{\mathrm{c}}\left(\mathrm{I}^{\mathrm{c}}\right)\mathrm{d}\lambda_{\mathrm{s}}=\frac{1}{2}\mathrm{k}^{\mathrm{c}}\int_{\lambda_{\mathrm{lb}}}^{\lambda_{\mathrm{ub}}}\mathrm{D}(\lambda_{\mathrm{s}})\left(\frac{\sqrt{\mathrm{I}^{\mathrm{c}}}}{\lambda_{\mathrm{s}}}-1\right)^2\mathrm{d}\lambda_{\mathrm{s}}, \tag{16}$$

where $D(\lambda_s)$ is represented by a scaled Beta distribution defined over $\lambda_s \in [\lambda_{lb}, \lambda_{ub}]$,

$$D(\lambda_s)=\begin{cases} \frac{y^{\alpha-1}(1-y)^{\beta-1}}{B(\alpha,\beta)(\lambda_{ub}-\lambda_{lb})}, & \text{for } y \in (0,1) \\ 0, & \text{otherwise} \end{cases}, \quad y=\frac{\lambda_s-\lambda_{lb}}{\lambda_{ub}-\lambda_{lb}}. \tag{17}$$

In the above expressions, α and β are the shape factors of Beta function that are related to the mean μ_r and standard deviation of σ_r the distribution through the following relations

$$\alpha=\mu_r'[\mu_r'-(\mu_r')^2-(\sigma_r')^2]/(\sigma_r')^2, \quad \beta=\alpha(1-\mu_r')/\mu_r', \tag{18}$$

$$\mu_r'=(\mu_r-\lambda_{lb})/(\lambda_{ub}-\lambda_{lb}), \quad \sigma_r'=\sigma_r/(\lambda_{ub}-\lambda_{lb}).$$

Assuming that the collagen fiber recruitment function $D(\lambda_s)$ does not vary with θ^c or z, the resulting tissue-level stress for large collagen fibers is obtained from Eqs. (16), $(11)_2$ and (7) as

$$\mathbf{S}^c=\frac{\phi^c k^c}{H}\int_0^H\int_{-\pi/2}^{\pi/2}\Gamma^c(\theta^c,z)\left[\int_{\lambda_{lb}}^{\lambda_{ub}}\frac{D(\lambda_s)}{\lambda_s^2}\left(1-\frac{\lambda_s}{\sqrt{I^c}}\right)d\lambda_s\right](\mathbf{n}^c\otimes\mathbf{n}^c)\,d\theta^c dz. \tag{19}$$

Figure 4 shows an example of the collagen fiber ensemble response $(S^c_{ens}-E_{ens})$ and the associated recruitment distribution $D(\lambda_s)$ for the equibiaxial loading path ($E_{11}=E_{22}$, $E_{12}=0$) with the definitions $E_{ens}=E_{11}$ and $S^c_{ens}=S^c_{11}+S^c_{22}$. This particular distribution indicates that most of the recruitment takes place at higher strains. The beginning and the end of the recruitment process are denoted in the figure by lower and upper bound strains, defined by $E_{lb}=(\lambda_{lb}^2-1)/2$ and $E_{ub}=(\lambda_{ub}^2-1)/2$, respectively. It is interesting to note that although individual collagen fibers are assumed to exhibit a linear behavior, the gradual straightening of the fibers produces an exponential-like stress-stretch relationship at both ensemble and tissue levels.

Strain energy form for myo-collagen coupling: In a pilot study (see Subsection 3.4) we observed that the fiber contributions Ψ^m and Ψ^c were not sufficient alone to fit to the biomechanical data. This finding provided additional evidence that the mechanical coupling between myofibers and collagen fibers is important and needs to be accounted for in the constitutive model. In particular, we found that, for the model without any interaction term, the regression residual was higher under equibiaxial loading condition (the r^2 value dropped by ~5% for the model without interaction term.) This residual was present in the regression analysis while all parameters associated with myo- and collagen fibers (i.e. $\{k_1^m, k_2^m, k^c, \mu_r, \sigma_r, \lambda_{lb}, \lambda_{ub}\}$) were subjected to optimization. This study suggested that an interaction term is missing from the constitutive model that cannot be compensated by modifying myo- and collagen fiber contributions alone. Recalling that the rotational

interactions are identically zero under equibiaxial loading condition, the study suggested that the missing interaction term is of extensional nature (i.e. a joint function of I^m and I^c.)

Accordingly, to capture the coupling between myofibers and (primary) collagen fibers, we propose to use an exponential energy form in terms of the additive variable $\tilde{I}=I^m+I^c/\lambda_s^2$. This form of energy was seen, in our pilot studies, to consistently enhance the capability of our model to capture the RVFW biomechanical behavior. Similar coupled invariants (without explicitly accounting for collagen fiber recruitment) have been used in the literature (Chatrchyan et al. 2012; Itskov et al. 2006; Schmid et al. 2009) to model biomechanical behavior of soft collagenous tissues. Note that the modified invariant I explicitly accounts for undulation of collagen fibers by using the invariant I^c/λ_s^2 instead of I^c alone. Indeed, we assumed that, similar to the mechanical contribution of large collagen fibers, the interaction between these fibers and myofibers occurs only after the collagen fibers are stretched beyond their slack stretches. This assumption entails two following conditions

$$\Psi_{\text{fiber}}^{\text{m-c}}\left(I^m, I^c\right)\Big|_{I^c\le\lambda_s^2}=0, \quad \frac{\partial\Psi_{\text{fiber}}^{\text{m-c}}\left(I^m, I^c\right)}{\partial \mathbf{C}}\Big|_{I^c\le\lambda_s^2}=\mathbf{0}, \tag{20}$$

for any arbitrary value of $I^m \ge 1$, where $\Psi_{\text{fiber}}^{\text{m-c}}\left(I^m, I^c\right)$ refers to the mechanical contribution of coupling between collagen fibers with a fixed slack stretch and myofibers. We propose the following exponential form for the coupling term $\Psi_{\text{fiber}}^{\text{m-c}}\left(I^m, I^c\right)$

$$\Psi_{\text{fiber}}^{\text{m-c}}\left(I^m, I^c\right)=\begin{cases}\frac{k_1^{mc}}{2k_2^{mc}}\psi\left(I^m, I^c\right) & I^m\ge 1, I^c\ge\lambda_s^2,\\ 0 & I^m>1, I^c\le\lambda_s^2,\end{cases} \tag{21}$$

where

$$\psi\left(I^m, I^c\right)=\left\{\exp\left[k_2^{mc}\left(\tilde{I}-2\right)\right]-\left[k_2^{mc}\left(I^c/\lambda_s^2-1\right)+1\right]\exp\left[k_2^{mc}(I^m-1)\right]\right\}, \tag{22}$$

and $k_1^{mc}>0$ and $k_2^{mc}>0$ are material parameters. (Note that the expression $\psi(I^m, I^c)$ is always positive for real variables). Again, similar to the case of collagen fibers, the energy function for coupling between an ensemble of myofibers and an ensemble of collagen fibers (with a distribution of slack stretch) takes the form

$$\Psi_{\text{ens}}^{\text{m-c}}\left(I^m, I^c\right)=\frac{k_1^{mc}}{2k_2^{mc}}\int_{\lambda_{lb}}^{\lambda_{ub}} D(\lambda_s)\psi\left(I^m, I^c\right)d\lambda_s. \tag{23}$$

Note that, in the above expression, $D(\lambda_s)$ is taken to be the same recruitment function used for large collagen fibers and defined in (17), because, as mentioned earlier, these fibers can

carry the stress induced by the coupling only when they are straightened. Making use of Eqs. (23), (12) and (7), the resulting stress tensor $\mathbf{S}^{\mathrm{m-c}}$ is given by

$$\mathbf{S}^{\mathrm{m-c}}=\frac{\phi^{\mathrm{c}}\mathrm{k}_1^{\mathrm{mc}}\,\mathrm{H}}{\mathrm{H}}\int_{0}^{\pi/2}\int_{-\pi/2-\theta_0^{\mathrm{c}}}^{\theta^{\mathrm{m}}+\theta_0^{\mathrm{c}}}\Gamma^{\mathrm{m}}\left(\theta^{\mathrm{m}},\mathrm{z}\right)\Gamma^{\mathrm{c}}\left(\theta^{\mathrm{c}},\mathrm{z}\right)\int_{\lambda_{\mathrm{lb}}}^{\lambda_{\mathrm{ub}}}\mathrm{D}(\lambda_{\mathrm{s}})\left\{\psi\left(\mathrm{I}^{\mathrm{m}},\mathrm{I}^{\mathrm{c}}\right)\mathbf{n}^{\mathrm{m}}\otimes\mathbf{n}^{\mathrm{m}}+\lambda_{\mathrm{s}}^{-2}\left\{\exp\left[\mathrm{k}_2^{\mathrm{mc}}(\tilde{\mathrm{I}}-2)\right]-\exp\left[\mathrm{k}_2^{\mathrm{mc}}\left(\mathrm{I}^{\mathrm{m}}-1\right)\right]\right\}\mathbf{n}^{\mathrm{c}}\otimes\mathbf{n}^{\mathrm{c}}\right\}\mathrm{d}\lambda_{\mathrm{s}}\mathrm{d}\theta^{\mathrm{c}}\mathrm{d}\theta^{\mathrm{m}}\mathrm{dz}. \tag{24}$$

We obtain the final expression for the total stress **S** by substituting equations (8), (14), (19), and (24) into equation (7). Finally, we note that we developed our model for the physiologically-relevant case when all or some of the fibers are stretched (characterized by the deformation range of $\mathrm{I}^{\mathrm{m}} > 1$ and $\mathrm{I}^{\mathrm{c}} > 1$ in fibers).

2.4 Parameter Estimation

Given the collected mechanical and the continuous transmural distributions (interpolated from histological measurements) data for the tissue-level behavior of the RVFW, our goal here is to determine best-fit parameters from the data via a rigorous parameter estimation algorithm. Assuming a plane stress state with $S_{33}=S_{13}=S_{23}=0$, the hydrostatic pressure in Eq. (8) is pre-determined as $p = k^g / C_{33}$. Note that all stress and strain components are given relative to the bases $\{\mathbf{e}_1, \mathbf{e}_2\}$ (Fig. 1). Since the biaxial strains were applied along material axes (Fig. 1), the measured shear stress S_{12} was negligible compared to the normal components S_{11} and S_{22} and not included in the optimization procedure. Making use of the nonlinear least squares procedure to estimate the parameters, we chose the following objective function Σ

$$\Sigma(\boldsymbol{\delta})=\sum_{\mathrm{i}=1}^{\mathrm{N}}\left[\left(\mathrm{S}_{11}-\hat{\mathrm{S}}_{11}(\boldsymbol{\delta})\right)^2+\left(\mathrm{S}_{22}-\hat{\mathrm{S}}_{22}(\boldsymbol{\delta})\right)^2\right]_{\mathrm{i}}, \tag{25}$$

where $\boldsymbol{\delta}=\{\mathrm{k}^{\mathrm{g}},\mathrm{k}_1^{\mathrm{m}},\mathrm{k}_2^{\mathrm{m}},\mathrm{k}^{\mathrm{c}},\mu_{\mathrm{r}},\sigma_{\mathrm{r}},\lambda_{\mathrm{lb}},\lambda_{\mathrm{ub}},\mathrm{k}_1^{\mathrm{mc}},\mathrm{k}_2^{\mathrm{mc}}\}$ denotes the set of unknown parameters, N is the total number of data points, and $\hat{\mathrm{S}}_{\mathrm{ij}}$ denotes the stress tensor component values obtained from the experimental biaxial tests. The optimal set of parameters then can be obtained via the minimization of the objective function (25)

$$\boldsymbol{\delta}^{*}:=\arg\left(\min_{\boldsymbol{\delta}}\Sigma(\boldsymbol{\delta})\right). \tag{26}$$

The minimization problem was solved using MATLAB function *lsqnonlin*, together with a trust-region-reflective algorithm. Our optimization procedure to estimate the parameters involved the following key steps:

1. Concerning the mechanical contribution of the matrix phase, we chose the small value of k^g = 10 kPa *a priori* because (I) the value of the (amorphous) matrix shear modulus is considered to be much lower than that of constituent fibers in

connective tissues (Humphrey 2002), and (II) its mass fraction is comparatively low as well.

2. As mentioned earlier, our previous experimental study (Hill et al. 2014) suggests that the nearly-linear behavior of the tissue in the low strain regime ($E^c < E_{lb}$) in the **S** − **E** space is entirely governed by the response of the myofibers as no collagen fiber is recruited in this regime. Taking advantage of these observations, we estimated the parameters E^{lb} and k_1^m directly from the experimental data in the low strain regime. (A similar approach was used in Fata et al. (2014).) The value of E_{lb} was obtained as the strain at which the transition from the initial linear to nonlinear behavior occurs indicating the initiation of collagen fiber recruitment. The value of k_1^m was estimated from the *intrinsic* fiber ensemble response ($S_{ens} - E_{ens}$), obtained from the equibiaxial loading path (where, again, $E_{ens} = E_{11}$ and $S_{ens} = S_{11} + S_{22}$). This response, as can be shown from Eqs. (14), (19), (24) together with conditions (2), is independent of the transmural myo- and collagen fiber splays.

3. Since the existing strain protocol 1:1 was not performed, this loading path was interpolated from all strain protocols for each specimen following our previous studies (Fata et al. 2014) (See Fig. 5(a) for a representative example of the interpolation.) Next, using the linearized form of the myofiber response in Eq. (13) for very small deformations (which is only a function of k_1^m), we were able to estimate the material parameter k_1^m from the (interpolated) ensemble response for the low strain regime ($E_{ens} < E_{lb}$), again, without using the transmural myofiber distribution (see Fig. 5(b) for a representative example of the fit to the interpolated equibiaxial data in the small strain regime.)

4. We did not include the parameter θ_0^c (defined in the interaction term (12)) in the optimization process, and we assigned a value to it, *a priori*. The final results in this work are given for the value $\theta_0^c = \pi/2$ (corresponding to the case that accounts for the interaction among all fiber ensembles in the same plane), however, further histological examination of the RVFW will be needed to acquire a more accurate estimate for this parameter.

5. In order to present the results as functions of strain, the unknown parameters λ_{lb} and λ_{ub} were replaced by E_{lb} and E_{ub}, as defined previously. Also, the corresponding changes were made in integrations (19) and (24), and also in relations (17) and (18) such that the reported values of μ_r and σ_r reflect the values in the strain space.

6. We used the multi-protocol strain-stress data for the entire strain range and histological data (Hill et al. 2014) for transmural myo- and collagen fiber orientation distributions to estimate the remaining unknown parameter using the optimization (26).

The summarized expressions for the stress components S_{11} and S_{22} in the biaxial test $\mathbf{F} = \mathrm{diag}(\lambda_1, \lambda_2, \lambda_1^{-1}\lambda_2^{-1})$ may be written in a concise notation as

$$\begin{pmatrix} S_{11} \\ S_{22} \end{pmatrix} = \phi^{g} k^{g} \left[1 - \begin{pmatrix} \lambda_1^{-4}\lambda_2^{-2} \\ \lambda_1^{-2}\lambda_2^{-4} \end{pmatrix} \right] + \frac{1}{H} \times \int_0^H \int_{-\pi/2}^{\pi/2} \left[\phi^{m} k_1^{m} \Gamma^{m} \left(1 - \frac{1}{\sqrt{I^{m}}} \right) e^{k_2^{m}(\sqrt{I^{m}}-1)^2} \mathbf{e}^{m} d\theta^{m} + \phi^{c} k^{c} \Gamma^{c} \int_{\lambda_{lb}}^{\lambda_{ub}} \frac{D}{\lambda_s^2} \left(1 - \frac{\lambda_s}{\sqrt{I^{c}}} \right) \mathbf{e}^{c} d\lambda_s d\theta^{c} \right] dz + \frac{\phi^{c} k_1^{mc}}{H} \int_0^H \int_{-\pi/2}^{\pi/2} \int_{-\pi/2}^{\pi/2} \Gamma^{m} \Gamma^{c} \int_{\lambda_{lb}}^{\lambda_{ub}} D \left[\mathbf{e}^{m} \psi + \lambda_s^{-2} \mathbf{e}^{c} \chi \right] d\lambda_s d\theta^{c} d\theta^{m} dz. \quad (27)$$

where $\mathbf{e}^{m,c} = [\cos(\theta^{m,c})^2, \sin(\theta^{m,c})^2]^T$ and $\chi = \exp[k_2^{mc}(\tilde{I} - 2)] - \exp[k_2^{mc}(I^{m} - 1)]$.

2.5 Post-estimation evaluation

2.5.1 Parameter correlations—Next, we studied the correlation between the contributions of different fiber types and the coupling. To quantify the correlations, we calculate the sensitivity matrix as follows

$$J_{ij} = \left. \frac{\Delta f_i}{\Delta \delta_j} \right|_{\text{Calculated at } \boldsymbol{\delta}^*}, \quad (28)$$

where δ^* denotes the vector of estimated parameters, and Δ denotes a variation in the respective variable. In this definition, and for the case of objective function (25), the vector **f** is defined as

$$\mathbf{f} = \{(S_{11})_1, (S_{11})_2, \ldots, (S_{11})_N, (S_{22})_1, (S_{22})_2, \ldots, (S_{22})_N\}. \quad (29)$$

The coefficient CR_{KL}, defining the correlation between the parameters δ_K and δ_L is then obtained as (Beck and Arnold 1977)

$$CR_{KL} = \frac{(M^{-1})_{KL}}{\sqrt{(M^{-1})_{KK}}\sqrt{(M^{-1})_{LL}}}, \quad (\text{no sum on k and L}). \quad (30)$$

where $\mathbf{M} = \mathbf{J}^T\mathbf{J}$.

2.5.2 Convexity of energy function—Convexity of the energy function $\Psi(\mathbf{C})$ in the right Cauchy-Green tensor **C** is important to ensure mathematical reliability of the energy function for numerical implementations (Holzapfel and Gasser 2000; Ogden 2003). As shown in Appendix A, the local convexity of energy function $\Psi(\mathbf{C})$ (defined in (6)) can be

examined through assessing local convexity of the ensemble energy (defined in (38)) with respect to invariants I^m and I^c.

3 Results

3.1 – Histological quantification

The 3D Beta-distribution surface fit the transmural histological data quite well for all (n=3) specimens, with the highest $r^2 \approx 0.96$ and the lowest $r^2 \approx 0.86$ (Fig. 6). We found that myo- and collagen fibers have a very close mean orientation at all depths (Fig. 7a), varying from approximately 10 deg at endocardium to −90 deg at the epicardial surface, and the average orientation is about −40 deg for both myo- and collagen fibers (Fig. 7a). However, the mean fiber orientation did not vary linearly along the transmural depth from endocardium (z=0) to epicardium (z=H) (Fig. 7a). The deviation from a linear behavior was more pronounced in the midwall region ($40 \leq z \leq 60$) and close the epicardium, although, for collagen fibers, the deviation was more noticeable close to endocardial surface as well (Fig. 7a). The change of mean fiber orientation in the RV (100 deg from Fig. 7) was lower than the corresponding value reported for the fiber orientation in the LV in rat (140 deg), however, considering that the RV is thinner than LV, the values of fiber orientation change per mm depth will be closer for the LV and RV. Moreover, collagen fibers showed a stronger deviation from the mean fiber orientation compared to myofibers except near to the epicardial and endocardial surfaces (Fig. 7b).

3.2 - Overall fit for mechanical testing data

The model fit the biaxial data very well, with the lowest $r^2 \approx 0.93$. Table 1 provides estimated values for all unknown constants and the associated r^2 values for five RVFW specimens. Myofiber modulus k_1^m (estimated directly from the low stain regime) showed lower variation than the constant k_2^m. Also, variations in the collagen fiber modulus k^c and the recruitment properties were generally low. In particular, the estimated values for lower and upper bound strains suggested that no collagen recruitment takes place below $E_{ens} = 0.03$ and all collagen are recruited beyond $E_{ens} = 0.24$. Moreover, the estimated values for constants μ_r and σ_r in the recruitment function $D(\lambda_s)$ suggested that most of the recruitment takes place towards to the upper strain bound E_{ub}.

A good fit was observed for all protocols (see Figs. 8a,b for stress-strain plots for Specimen No. 1). The values for S_{11} were generally higher than that of S_{22}. This is consistent with the fact that the axis $\mathbf{e}_1$ is nearly aligned with the mean direction for myo- and collagen fibers (see Fig. 1a). Another interesting finding was that the stress values for the protocol 1 (the closer one to the equibiaxial path) tend to be higher (Fig. 8). This observation is also consistent with the assumption that fibers do not rotate under equibiaxial loading condition, and therefore, they stiffen quicker versus the case that they are subjected to non-equibiaxial loading conditions. Finally, high quality fits were obtained for the remaining RVFW specimens.

3.3. - Prediction based on equibiaxial fit

As mentioned earlier, we interpolated the data for the equibiaxial loading path ($E_{11} = E_{22} = E_{ens}$) from experimentally acquired multiprotocol data. An example of this interpolation was shown in Fig. 5(a). Interestingly, we found that if we quantify our model only using the interpolated equibiaxial data, the quantified model can still (at least qualitatively) capture the stress-strain behavior in all protocols used for the interpolation (see Fig. 9 for a representative example). This finding is consistent with the results of Sacks (2003) on modeling the mechanical behavior of pericardium. In particular, he quantified a two-parameter model entirely from equibiaxial test data, and predicted the behavior of the tissue under non-equibiaxial loading conditions with an excellent agreement.

3.4 - Fiber contributions and fiber-fiber interactions

The constitutive model (6) without the interaction term $\Psi^{m\text{-}c}$ was not sufficient to consistently fit the biomechanical testing data. In particular, the model (6) without the term $\Psi^{m\text{-}c}$ had its greatest fitting residual under (nearly) equibiaxial loading conditions (where the interactions would be greatest), and the residual reduced for loading conditions far from the equibiaxial loading path (Fig. 10). The inclusion of the interaction term $\Psi^{m\text{-}c}$ in the constitutive model (6) notably improved the fit, especially under (nearly) equibiaxial loading conditions. The r^2 value increased from 0.93 to 0.98 and the rms value dropped from 3.30 to 1.75 (kPa) for the equibiaxial loading protocol with the p-value being 0.021 between the residual errors of two models.

Next, using the complete model we investigated the prediction of our model for mechanical contribution of myo- and collagen fibers and the interaction among them in the total energy density function under equibiaxial loading condition (Fig. 11). We found that in the low strain regime, where most of collagen fibers are still undulated, the behavior of the RVFW is governed by myofiber response. However, collagen fibers and their interaction with myofibers begin to gradually contribute to the behavior as their recruitment proceeds. Once fully straightened, the collagen fibers become a major contributor to the RVFW behavior. We further investigated the predictions of our model for contributions of myo- and collagen fibers and the interaction in the total stress as functions of strain (Fig. 12). Consistent with our observation for the case of energy function described in the context of previous figure, collagen fibers and their interaction with myofibers begin to gradually contribute to accommodate mechanical stress along with the recruitment progression, for all three loading conditions (Fig. 12). In particular, the collagen fibers become the greater contributor to the RVFW behavior for the case of equibiaxial path (Figs. 12a,b). Interestingly, the contribution of the interaction is the highest under equibiaxial loading condition as well (Figs. 12a,b). In particular, an average ratio of the interaction part of the stress to the total stress $((S_{11}^{m-c}+S_{22}^{m-c})/(S_{11}+S_{22}))$ at the highest strains was 20%, 12% and 6% for the loading path $E_{11} = E_{22}$ (Figs. 12a,b), $E_{11} = 2E_{22}$ (Figs. 12c,d), and $E_{11} = 0.5E_{22}$ (Figs. 12e,f), respectively. Finally, we note that the energy and stress contributions of the matrix were comparatively insignificant and not included in Figs. 11 and 12.

3.5 - Parameter correlations and convexity

The sensitivity matrix columns were calculated by varying each of the parameters in a range of ± 5% around their estimated values, while the remaining parameters are kept constant (see Table 2 for correlation coefficients between the selected parameters $\boldsymbol{\kappa}=\{k_1^m, k_2^m, k^c, k_1^{mc}, k_2^{mc}\}$ for estimated values of Specimen No. 3.) The closer the absolute value of CR_{KL} is to 1, the higher is the correlation between the parameters $\boldsymbol{\kappa}_K$ and $\boldsymbol{\kappa}_L$. Also, the total energy function $\Psi(\mathbf{C})$ satisfied the local convexity condition for all specimens. The constant contours of the energy function $\Psi^*_{ens}(I^m, I^c)$, defined in (38), were convex in I^m and I^c for all specimens within the range of defamation examined in this paper (see Fig. 13 for a representative example). As shown in Appendix A, the convexity of $\Psi^*_{ens}(I^m, I^c)$ in in I^m and I^c implies the local convexity of $\Psi(\mathbf{C})$ in $\mathbf{C}$.

3.6 - Sensitivity to full 3D transmural fiber orientation

Finally, it is interesting to examine the sensitivity of our model to the distributions $\Gamma^m(\theta^m, z)$ and $\Gamma^c(\theta^c, z)$ by comparing the results of our model with those based on the approximation of "average" fiber direction. Along these lines, we define the following structural tensors characterizing "average" orientation of myo- and collagen fiber

$$\mathbf{H}^m=\frac{1}{H}\int_0^H\int_{-\pi/2}^{\pi/2}\Gamma^m(\theta^m,z)\,(\mathbf{n}^m\otimes\mathbf{n}^m)\,d\theta^m dz,\quad \mathbf{H}^c=\frac{1}{H}\int_0^H\int_{-\pi/2}^{\pi/2}\Gamma^c(\theta^c,z)\,(\mathbf{n}^c\otimes\mathbf{n}^c)\,d\theta^c dz, \tag{31}$$

respectively. Then, a new energy function based on the structural tensors can be written as (Gasser et al. 2006; Holzapfel and Gasser 2000)

$$\Psi^{ST}(\mathbf{C})=\phi^g\Psi^g(I_1)+\phi^m\Psi^m_{ens}(\bar{I}^m)+\phi^c\left[\Psi^c_{ens}(\bar{I}^c)+\Psi^{m-c}_{ens}(\bar{I}^m,\bar{I}^c)\right], \tag{32}$$

where = $\bar{I}^m = \mathbf{H}^m:\mathbf{C}$ and $\bar{I}^c = \mathbf{H}^c:\mathbf{C}$, and the superscript "ST" refers to the "structural tensor" model. We conducted comparisons between the results of our model with those based on the energy function (32) for the stress-strain behavior of the RV myocardium (Fig. 14). The results were calculated for the estimated values of Specimen No. 3 in Table 1 for multiple loading paths. We observed that the results of two models coincided for the case of equibiaxial loading path (because the fibers do not rotate under this condition.) However, for non-equibiaxial loading conditions of the form $E_{11} = \upsilon E_{22}$ (where $\upsilon > 1$ is a constant), the results of the "structural tensor" model notably underestimated the results of our model for S_{11}, while they tend to overestimate the results of our model for S_{22}. We observed the opposite for the loading conditions of the form $E_{22} = \upsilon E_{11}$ (again, with $\upsilon > 1$). These findings are consistent with the results of Bischoff et al. (Bischoff 2006).

4 Discussion

4.1 – Overall findings

In this work, we took an essential step towards the modeling the biomechanical behavior of passive RVFW myocardium by formulating a structurally-informed constitutive model for the RVFW and conducting detailed parameter estimation. A distinctive feature of this work was the use of a structurally-based constitutive model that accounts for the myofiber-collagen fiber interactions. The construction and quantification of such a model that accounts for detailed and histologically-measured information on the structure of the tissue is an important step towards development of constitutive models that offer a powerful predictive capability. Our structurally-informed constitutive model was also formulated in an invariant-based form that is more suitable for numerical implementations, similar to the previous models proposed for the passive mechanical behavior of the myocardium (Holzapfel and Ogden 2009; Humphrey and Yin 1987; Sacks and Chuong 1993). Our modeling also provides a framework to develop multi-scale models of pressure-induced growth and remodeling of the RV myocardium under PAH. Accordingly, our long-term goal is to implement such models in a finite-element heart model to facilitate diagnosis and prognosis of PAH disease, as well as to lay out foundation to develop therapies specifically targeting improving RV response to PAH. In the following, we discuss the results presented in this work.

4.2 - Insights into structure-function relationship

Under biaxial tensile loading condition and within the strain range of E_{11}, $E_{22} < 0.3$, all RVFW tissue specimens exhibited highly nonlinear and anisotropic stress-strain relationship with a pronounced stiffening along the mean fiber direction. The anisotropic behavior of the RVFW was evident from the results of strain protocols close to the equibiaxial loading path where the stress component S_{11} has a notably higher value than that of S_{22}. This was consistent with histological data for the transmural fiber orientation indicating that the mean fiber direction was nearly aligned with $\mathbf{e}_1$ - direction (see Fig. 1). However, histological data revealed that local microstructural axes of the RVFW are not generally orthogonal, and therefore, the behavior of the RVFW cannot be assumed to be locally orthotropic. This is in contrast to the assumption of locally orthotropic behavior in constitutive modeling of the passive behavior of the LV myocardium frequently used in the literature (Costa et al. 2001; Schmid et al. 2006). Moreover, we found that the mean fiber orientation did not vary linearly along the transmural depth from endocardium (z=0) to epicardium (z=H) (Fig. 7a). This is consistent with the finding for transmural orientation of myofibers in LV myocardium for human (Holzapfel et al. 2007), dog (Streeter et al. 1969), and pig (Streeter 1979).

For general biaxial strain protocols, our investigation revealed a high sensitivity of the model to the transmural fiber orientation distribution. This was expected as both myo- and collagen fibers exhibited a strong 3D orientation dispersion throughout the RVFW specimens. However, under equibiaxial loading condition, the results of our model suggest that simpler phenomenological models based on mean fiber orientations should be able to capture the biomechanical behavior of the RVFW. Another structural insight from our analysis was that the nonlinear behavior of the RVFW appears to be derived from two sources: (I) gradual

recruitment of collagen fibers which produces an exponential-like behavior, and (II) stiffening of myofibers as they experience larger deformation than collagen fibers because of their minimal undulation. As mentioned earlier, gaining insights into the contribution of each type of fiber to the biomechanical behavior of the RVFW is important for the long-term goal of understanding and modeling structural adaptations of the RVFW under cardiopulmonary disorders. In this connection, it is worth clarifying the contrast between our model with the existing constitutive models for myocardium such as the strain-based model by Costa et al. (2001) and the invariant-based model by Holzapfel and Ogden (2009). Such models have been proven successful in capturing overall mechanical behavior of (left ventricular) myocardium and they are also quite tractable for the use in organ-level simulations. However, their applicability in studying and understanding the mechanical role of each fiber type, and more importantly, adaptations experienced by each fibrous constituent during pathological conditions is limited. For such applications, we believe our model with detailed fiber-specific features can provide a better description of underlying mechanical and structural mechanisms.

4.3 – Are interactions important?

Perhaps the most novel finding in the present study was the substantial mechanical coupling between myofibers and large collagen fibers. Indeed, our pilot studies suggested that the inclusion of an interaction term Ψ^{m-c} is necessary to consistently capture the behavior of the RVFW under various loading states (Fig. 10). In particular, the constitutive model without the interaction term had its greatest fitting residual for the equibiaxial loading protocol (Fig. 10) suggesting that a key interaction term that is missing should be of extensional nature (i.e. a joint function of I^m and I^c) because the change of angle between fiber directions $\mathbf{n}^m$ and $\mathbf{n}^c$ is zero under equibiaxial loading condition. Similar findings on existence of interactions between structural constituents of cardiac tissues was reported in the constitutive modeling of the left ventricle myocardium (Holzapfel and Ogden 2009) and exogenously cross-linked pericardium (Sacks et al. 2016). The parametric study of the quantified model further suggests that the strongest coupling takes place under equibiaxial loading condition (Figs. 11 and 12). Making contact with our histological study of the RVFW, we hypothesized that this coupling could be in part due to the existence of a rather dense network of fine collagen fiber network running across myofibers and large collagen fibers.

Moreover, we investigated the existence of similar type of interaction between ensembles of myofibers in the low strain regime (see Appendix B), but did not detect any coupling. This inspection also supports the outcome of our parameter estimations in the sense that the coupling between myofiber and (large) collagen fibers stem from the existence of another collagenous fiber phase that started to contribute to the overall behavior of the RVFW in the larger strain regime. Our work was an attempt to account for this collagenous phase in a tissue-level sense. Our findings put forth the need for more advanced histological studies of endomysial and perimysial collagen fibers to directly account for both types of collagen fibers in the constitutive modeling of the RVFW.

4.4 –Identifiability of parameters and convexity of the energy function

The calculated correlation coefficients listed in Table 2 show that the parameter k_1^m is in moderate correlation with k_2^m, in low correlation with k^c, and in nearly in no correlation with k_1^{mc} and k_2^{mc}. However, recalling that k_1^m was estimated independently from the low strain regime data, the moderate correlation between $k_1^m$and k_2^m did not pose a problem in our parameter estimation. In other words, there was no correlation between k_1^m and k_2^m in low strain regime. Moreover, the low correlations between k_1^m, k^c, and k_1^m could indicate that the model has been able to sufficiently decouple the effect of myofibers from collagen fibers and from the interaction between myofiber and collagen fibers. In contrast, the correlation between k_1^{mc} and k_2^{mc} was very high. This very high correlation would pose some difficulties in quantifying these two parameters unambiguously. However, the very low correlation between k^c and k_1^{mc} (and k_2^{mc}) allows to quite accurately estimate the effective contribution of the interaction term Ψ^{m-c}, although the uniqueness of the estimated values for k_1^{mc} and k_2^{mc} is questionable. Overall, we found in our parameter estimation that the contribution of Ψ^{m-c} was secondary with respect to Ψ^c. Finally, we investigated the convexity of the total energy function $\Psi(\mathbf{C})$ with respect to $\mathbf{C}$. We found that the total energy is convex in $\mathbf{C}$ for all five sets of estimated values shown in Table 1 and within the relevant physiological range (E_{11}, $E_{22} < 0.3$), although the interaction term Ψ^{m-c} $\mathbf{C}$ alone is not convex in $\mathbf{C}$. The total convex property of $\Psi(\mathbf{C})$ indicates its acceptability for computational implementations.

5 Conclusion and future studies

In this study, the 3D transmural fiber orientation for both myo- and collagen fibers in viable specimens of healthy murine RVFW was presented. The distributions were directly incorporated into a structure-based constitutive model that accounts for mechanical contribution of each fiber type separately, and the interaction among them. It was demonstrated that the model equipped with the quantitative transmural distributions excellently fit the multi-protocol biaxial test mechanical data for similar healthy RVFW specimens (Hill et al. 2014). In addition, the model was able to quite accurately predict the behavior of the specimen under non-equibiaxial loading protocols when quantified only through interpolated equibiaxial loading data. To our best knowledge, this is the first study to investigate the contribution of each fiber type and interaction among them in the mechanical behavior of myocardial tissues based on transmural orientation distributions for each fiber type.

The results of this study will be particularly useful for predicting the response of the myocardium under pulmonary arterial hypertension (PAH) disorder. More specifically, our model can be used to elucidate how mechanical and structural characteristics of the myocardium adapt to a chronic pressure overload, and what effects this adaptation has at tissue- and organ-level behaviors. As an important feature for this purpose, our structural approach allows decoupling the relative effects of myofiber hypertrophy from changes in collagen fiber orientation, in relation to the tissue-level behavior. Ultimately, further development and implementation of our model in patient-specific organ-level simulations

will allow investigation of optimal diagnosis, new individualized interventions and treatment protocols for PAH.

Acknowledgments

This work was supported by the U.S. National Institutes of Health grants 1F32 HL132543 to R.A. and 1F32 HL117535 to M.H.

Appendix A

In this appendix, we discuss the local convexity of the energy function $\Psi(\mathbf{C})$ with respect to the right Cauchy-Green tensor $\mathbf{C}$. Recalling from relation (6) that the ground matrix term Ψ^{g} is neo-Hookean and convex in $\mathbf{C}$, it suffices to only assess the convexity of the anisotropic part of the energy, given by

$$\Psi^{\mathrm{Aniso}}(\mathbf{C})=\phi^{\mathrm{m}}\Psi^{\mathrm{m}}(\mathbf{C})+\phi^{\mathrm{c}}\left[\Psi^{\mathrm{c}}(\mathbf{C})+\Psi^{\mathrm{m-c}}(\mathbf{C})\right]. \quad (33)$$

By definition, the local convexity of $\Psi^{\mathrm{Aniso}}(\mathbf{C})$ requires that the fourth-order tensor $\mathbf{L} = \partial^2\Psi^{\mathrm{Aniso}}(\mathbf{C}) / \partial\mathbf{C}\partial\mathbf{C}$ be positive-semi definite, i.e.

$$\mathbf{A}\cdot\mathbf{L}\mathbf{A}\geq 0, \quad (34)$$

for all second order tensors $\mathbf{A}$. We note that, although the tensor $\mathbf{C}$ is subjected to the incompressibility constraint $\det(\mathbf{C})=1$, we investigate the convexity of $\Psi(\mathbf{C})$ in two-dimensional matrix $\mathbf{C}$ with three independent components in the plane containing the unit vectors $\mathbf{n}^{\mathrm{m}}$ and $\mathbf{n}^{\mathrm{c}}$.

Substituting the energy expressions in relations (11) and (12) into (33), it follows that

$$\begin{aligned}\Psi^{\mathrm{Aniso}}(\mathbf{C})=\frac{1}{\mathrm{H}}\int_0^{\mathrm{H}}\Bigg[&\phi^{\mathrm{m}}\int_{-\pi/2}^{\pi/2}\Gamma^{\mathrm{m}}(\theta^{\mathrm{m}},\mathrm{z})\,\Psi^{\mathrm{m}}_{\mathrm{ens}}(\mathrm{I}^{\mathrm{m}})\,\mathrm{d}\theta^{\mathrm{m}}\mathrm{dz}+\phi^{\mathrm{c}}\int_{-\pi/2}^{\pi/2}\Gamma^{\mathrm{c}}(\theta^{\mathrm{c}},\mathrm{z})\,\Psi^{\mathrm{c}}_{\mathrm{ens}}(\mathrm{I}^{\mathrm{c}})\,\mathrm{d}\theta^{\mathrm{c}}\mathrm{dz}\\&+\phi^{\mathrm{c}}\int_{-\pi/2}^{\pi/2}\int_{-\pi/2}^{\pi/2}\Gamma^{\mathrm{m}}(\theta^{\mathrm{m}},\mathrm{z})\,\Gamma^{\mathrm{c}}(\theta^{\mathrm{c}},\mathrm{z})\,\Psi^{\mathrm{m-c}}_{\mathrm{ens}}(\mathrm{I}^{\mathrm{m}},\mathrm{I}^{\mathrm{c}})\,\mathrm{d}\theta^{\mathrm{c}}\mathrm{d}\theta^{\mathrm{m}}\Bigg]\mathrm{dz},\end{aligned} \quad (35)$$

in which use has been made of $\theta_0^{\mathrm{c}}=\pi/2$. Recalling that the distribution functions Γ^{m} and Γ^{c} satisfy the condition (5), it is easy to see that the convexity of the above expression in $\mathbf{C}$ is equivalent to the convexity of the function

$$\begin{aligned}\Psi^{*}(\mathrm{I}^{\mathrm{m}},\mathrm{I}^{\mathrm{c}};\mathrm{R}^{\mathrm{m}},\mathrm{R}^{\mathrm{c}})=&\phi^{\mathrm{m}}\int_{-\pi/2}^{\pi/2}\mathrm{R}^{\mathrm{m}}(\theta^{\mathrm{m}})\,\Psi^{\mathrm{m}}_{\mathrm{ens}}(\mathrm{I}^{\mathrm{m}})\,\mathrm{d}\theta^{\mathrm{m}}+\phi^{\mathrm{c}}\int_{-\pi/2}^{\pi/2}\mathrm{R}^{\mathrm{c}}(\theta^{\mathrm{c}})\,\Psi^{\mathrm{c}}_{\mathrm{ens}}(\mathrm{I}^{\mathrm{c}})\,\mathrm{d}\theta^{\mathrm{c}}\\&+\phi^{\mathrm{c}}\int_{-\pi/2}^{\pi/2}\int_{-\pi/2}^{\pi/2}\mathrm{R}^{\mathrm{m}}(\theta^{\mathrm{m}})\,\mathrm{R}^{\mathrm{c}}(\theta^{\mathrm{c}})\,\Psi^{\mathrm{m-c}}_{\mathrm{ens}}(\mathrm{I}^{\mathrm{m}},\mathrm{I}^{\mathrm{c}})\,\mathrm{d}\theta^{\mathrm{c}}\mathrm{d}\theta^{\mathrm{m}},\end{aligned} \quad (36)$$

where $\mathrm{R}^{\mathrm{m}}(\Theta)$ and $\mathrm{R}^{\mathrm{c}}(\Phi)$ are two distribution functions satisfying the condition (5). Making use of this condition, the above energy function can be rewritten as

$$\Psi^{*}\left(\mathrm{I}^{\mathrm{m}},\mathrm{I}^{\mathrm{c}};\mathrm{R}^{\mathrm{m}},\mathrm{R}^{\mathrm{c}}\right)=\int_{-\pi/2}^{\pi/2}\int_{-\pi/2}^{\pi/2}\mathrm{R}^{\mathrm{m}}\left(\theta^{\mathrm{m}}\right)\mathrm{R}^{\mathrm{c}}\left(\theta^{\mathrm{c}}\right)\Psi_{\mathrm{ens}}^{*}\left(\mathrm{I}^{\mathrm{m}},\mathrm{I}^{\mathrm{c}}\right)\mathrm{d}\theta^{\mathrm{m}}\mathrm{d}\theta^{\mathrm{c}}, \tag{37}$$

with

$$\Psi_{\mathrm{ens}}^{*}(\mathrm{I}^{\mathrm{m}},\mathrm{I}^{\mathrm{c}})=\phi^{\mathrm{m}}\Psi_{\mathrm{ens}}^{\mathrm{m}}(\mathrm{I}^{\mathrm{m}})+\phi^{\mathrm{c}}[\,\Psi_{\mathrm{ens}}^{\mathrm{c}}(\mathrm{I}^{\mathrm{c}})+\Psi_{\mathrm{ens}}^{\mathrm{m-c}}(\mathrm{I}^{\mathrm{m}},\mathrm{I}^{\mathrm{c}})]. \tag{38}$$

Therefore, it follows that the convexity of the function $\Psi_{\mathrm{ens}}^{*}(\mathrm{I}^{\mathrm{m}},\mathrm{I}^{\mathrm{c}})$ in **C** implies the convexity of $\Psi^{\mathrm{Aniso}}(\mathbf{C})$. In other words, $\Psi^{\mathrm{Aniso}}(\mathbf{C})$ is convex if the tensor $\mathbf{L}^{*}=\partial^{2}\Psi_{\mathrm{ens}}^{*}(\mathrm{I}^{\mathrm{m}},\mathrm{I}^{\mathrm{c}})/\partial\mathbf{C}\partial\mathbf{C}$ is positive-semi definite. The tensor $\mathbf{L}^{*}$ is obtained as

$$\mathbf{L}^{*}=(\Psi_{\mathrm{ens}}^{*})_{,\mathrm{I}^{\mathrm{m}}\mathrm{I}^{\mathrm{m}}}\,\mathbf{n}^{\mathrm{m}}\otimes\mathbf{n}^{\mathrm{m}}\otimes\mathbf{n}^{\mathrm{m}}\otimes\mathbf{n}^{\mathrm{m}}+(\Psi_{\mathrm{ens}}^{*})_{,\mathrm{I}^{\mathrm{c}}\mathrm{I}^{\mathrm{c}}}\,\mathbf{n}^{\mathrm{c}}\otimes\mathbf{n}^{\mathrm{c}}\otimes\mathbf{n}^{\mathrm{c}}\otimes\mathbf{n}^{\mathrm{c}}+(\Psi_{\mathrm{ens}}^{*})_{,\mathrm{I}^{\mathrm{m}}\mathrm{I}^{\mathrm{c}}}(\mathbf{n}^{\mathrm{m}}\otimes\mathbf{n}^{\mathrm{m}}\otimes\mathbf{n}^{\mathrm{c}}\otimes\mathbf{n}^{\mathrm{c}}+\mathbf{n}^{\mathrm{c}}\otimes\mathbf{n}^{\mathrm{c}}\otimes\mathbf{n}^{\mathrm{m}}\otimes\mathbf{n}^{\mathrm{m}}), \tag{39}$$

in which subscript commas followed by an index denote derivatives with respect to the corresponding variables. Making use of the above expression, the condition (34) can be written as

$$\mathrm{a}_{1}^{2}(\Psi_{\mathrm{ens}}^{*})_{,\mathrm{I}^{\mathrm{m}}\mathrm{I}^{\mathrm{m}}}+\mathrm{a}_{2}^{2}(\Psi_{\mathrm{ens}}^{*})_{,\mathrm{I}^{\mathrm{c}}\mathrm{I}^{\mathrm{c}}}+2\mathrm{a}_{1}\mathrm{a}_{2}(\Psi_{\mathrm{ens}}^{*})_{,\mathrm{I}^{\mathrm{m}}\mathrm{I}^{\mathrm{c}}}\geq 0, \tag{40}$$

where $\mathrm{a}_1 = \mathbf{n}^{\mathrm{m}}\cdot\mathbf{A}\mathbf{n}^{\mathrm{m}}$ and $\mathrm{a}_2 = \mathbf{n}^{\mathrm{c}}\cdot\mathbf{A}\mathbf{n}^{\mathrm{c}}$. The above condition can be further recast into

$$\begin{pmatrix}\mathrm{a}_1\\ \mathrm{a}_2\end{pmatrix}\cdot\begin{pmatrix}(\Psi_{\mathrm{ens}}^{*})_{,\mathrm{I}^{\mathrm{m}}\mathrm{I}^{\mathrm{m}}} & (\Psi_{\mathrm{ens}}^{*})_{,\mathrm{I}^{\mathrm{m}}\mathrm{I}^{\mathrm{c}}}\\ (\Psi_{\mathrm{ens}}^{*})_{,\mathrm{I}^{\mathrm{m}}\mathrm{I}^{\mathrm{c}}} & (\Psi_{\mathrm{ens}}^{*})_{,\mathrm{I}^{\mathrm{c}}\mathrm{I}^{\mathrm{c}}}\end{pmatrix}\begin{pmatrix}\mathrm{a}_1\\ \mathrm{a}_2\end{pmatrix}\geq 0, \tag{41}$$

which is always satisfied for arbitrary real values of a_1 and a_2 if $\Psi_{\mathrm{ens}}^{*}(\mathrm{I}^{\mathrm{m}},\mathrm{I}^{\mathrm{c}})$ is locally convex in I^{m} and I^{c} jointly. Two conditions to guarantee the convexity of $\Psi_{\mathrm{ens}}^{*}(\mathrm{I}^{\mathrm{m}},\mathrm{I}^{\mathrm{c}})$ are

$$(\Psi_{\mathrm{ens}}^{*})_{,\mathrm{I}^{\mathrm{m}}\mathrm{I}^{\mathrm{m}}}\geq 0,\qquad (\Psi_{\mathrm{ens}}^{*})_{,\mathrm{I}^{\mathrm{m}}\mathrm{I}^{\mathrm{m}}}(\Psi_{\mathrm{ens}}^{*})_{,\mathrm{I}^{\mathrm{c}}\mathrm{I}^{\mathrm{c}}}-\left[(\Psi_{\mathrm{ens}}^{*})_{,\mathrm{I}^{\mathrm{m}}\mathrm{I}^{\mathrm{c}}}\right]^{2}\geq 0. \tag{42}$$

It is further simple to show that $(\Psi_{\mathrm{ens}}^{*})_{,\mathrm{I}^{\mathrm{m}},\mathrm{I}^{\mathrm{m}}}$ is positive for the ensemble energy functions proposed in this work for all deformation (under the aforementioned conditions of positive material parameters.) The remaining condition $(42)_2$ will be satisfied if

$$\left\{\frac{\phi^{m}k_1^{m}}{2I^{m}}\exp\left[k_2^{m}\left(\sqrt{I^{m}}-1\right)^2\right]\left[2k_2^{m}\left(\sqrt{I^{m}}-1\right)^2+1/\sqrt{I^{m}}\right]+\phi^{c}k_1^{mc}k_2^{mc}\int_{\lambda_{lb}}^{\lambda_{ub}}D(\lambda_s)\psi d\lambda_s\right\}$$
$$\times\phi^{c}\left\{\frac{k^{c}}{2I^{c}\sqrt{I^{c}}}\int_{\lambda_{lb}}^{\lambda_{ub}}\frac{D(\lambda_s)}{\lambda_s}d\lambda_s+k_1^{mc}k_2^{mc}\int_{\lambda_{lb}}^{\lambda_{ub}}\frac{D(\lambda_s)}{\lambda_s^4}\exp\left[k_2^{mc}(\tilde{I}-2)\right]d\lambda_s\right\}$$
$$-\left\{\phi^{c}k_1^{mc}k_2^{mc}\int_{\lambda_{lb}}^{\lambda_{ub}}\frac{D(\lambda_s)}{\lambda_s^2}\left\{\exp\left[k_2^{mc}(\tilde{I}-2)\right]-\exp\left[k_2^{mc}(I^{m}-1)\right]\right\}d\lambda_s\right\}^2\geq 0, \quad (43)$$

where the function $\psi\ (I^{m}, I^{c})$ is given in (22).

Appendix B

Here, we express the energy term Ψ^{m-m} used to detect possible interactions between myofiber ensembles in the low strain regime (where Ψ^{c} and Ψ^{m-c} do not contribute) as follows

$$\Psi^{m-m}=\frac{1}{H}\frac{k_1^{m-m}}{2k_2^{m-m}}\int_0^{H}\left\{\int_{-\pi/2}^{\pi/2}\int_{-\pi/2}^{\pi/2}\Gamma^{m}(\theta^{m},Z)\,\Gamma^{m}(\theta^{m*},Z)\left\{\exp\left[k_2^{m-m}\left(\sqrt{I^{m}+I^{m*}}-\sqrt{2}\right)^2\right]-1\right\}d\theta^{m}d\theta^{m*}\right.$$
$$\left.-\int_{-\pi/2}^{\pi/2}\left[\Gamma^{m}(\theta^{m},z)\right]^2\left\{\exp\left[2k_2^{m-m}\left(\sqrt{I^{m}}-1\right)^2\right]-1\right\}d\theta^{m}\right\}dz. \quad (44)$$

In the above expression, k_1^{m-m} and k_2^{m-m} are unknown parameters, and the angular variables Θ^{m} and Θ^{m*} (associated with invariants I^{m} and I^{m*}) have been used to differentiate two myofiber ensembles with different orientations. The second term in the above expression subtracts the energy for the case of $\Theta^{m} = \Theta^{m*}$ accounted for in the first term (enforcing that each myofiber ensemble does not interact with itself.)

References

Beck, JV., Arnold, KJ. Parameter estimation in engineering and science. James Beck; 1977.

Bischoff JE. Continuous versus discrete (invariant) representation of fibrous structures for modeling nonlinear anisotropic soft tissue behavior. International Journal of Non-Linear Mechanics. 2006; 41:167–179.

Bogaard HJ, Abe K, Vonk Noordegraaf A, Voelkel NF. The right ventricle under pressure: cellular and molecular mechanisms of right-heart failure in pulmonary hypertension. Chest. 2009; 135:794–804. [PubMed: 19265089]

Borg TK, Caulfield JB. The collagen matrix of the heart. Fed Proc. 1981; 40:2037–2041. [PubMed: 7227559]

Borg TK, Johnson LD, Lill PH. Specific attachment of collagen to cardiac myocytes: in vivo and in vitro. Developmental biology. 1983; 97:417–423. [PubMed: 6852372]

Caulfield JB, Borg TK. The collagen network of the heart. Lab Invest. 1979; 40:364–372. [PubMed: 423529]

Champion HC, Michelakis ED, Hassoun PM. Comprehensive invasive and noninvasive approach to the right ventricle-pulmonary circulation unit: state of the art and clinical and research implications. Circulation. 2009; 120:992–1007. [PubMed: 19752350]

Chatrchyan S, et al. Observation of a new boson at a mass of 125 GeV with the CMS experiment at the LHC. Phys Lett B. 2012; 716:30–61. doi.

Costa KD, Holmes JW, MeCulloch AD. Modelling cardiac mechanical properties in three dimensions. Phil Trans R Soc Lond. 2001; 359:1233–1250.

Courtney T, Sacks MS, Stankus J, Guan J, Wagner WR. Design and analysis of tissue engineering scaffolds that mimic soft tissue mechanical anisotropy. Biomaterials. 2006; 27:3631–3638. [PubMed: 16545867]

Dokos S, Smaill BH, Young AA, LeGrice IJ. Shear properties of passive ventricular myocardium. Am J Physiol Heart Circ Physiol. 2002; 283:H2650–H2659. [PubMed: 12427603]

Fan R, Sacks MS. Simulation of planar soft tissues using a structural constitutive model: finite element implementation and validation. J Biomech. 2014; 47:2043–2054. [PubMed: 24746842]

Fata B, Zhang W, Amini R, Sacks M. Insights into Regional Adaptations in the Growing Pulmonary Artery Using a Meso-Scale Structural Model: Effects of Ascending Aorta Impingement. J Biomech Eng. 2014

Forfia PR, et al. Tricuspid annular displacement predicts survival in pulmonary hypertension. American journal of respiratory and critical care medicine. 2006; 174:1034–1041. [PubMed: 16888289]

Forfia PR, et al. Hyponatremia predicts right heart failure and poor survival in pulmonary arterial hypertension. American journal of respiratory and critical care medicine. 2008; 177:1364–1369. [PubMed: 18356560]

Fox CC, Hutchins GM. The Architecture of the Human Ventricular Myocardium Hopkins. Medical Journal. 1972; 130:289–299.

Fung, YC. Biomechanics: Mechanical Properties of Living Tissues. 2nd. New York: Springer Verlag; 1993.

Gasser TC, Ogden RW, Holzapfel GA. Hyperelastic modelling of arterial layers with distributed collagen fibre orientations. J R Soc Interface. 2006; 3:15–35. doi:3253307783333263 [pii] 10.1098/rsif.2005.0073. [PubMed: 16849214]

Hasenkam JM, Nygaard H, Paulsen PK, Kim WY, Hansen OK. What force can the myocardium generate on a prosthetic mitral valve ring? An animal experimental study. J Heart Valve Dis. 1994; 3:324–329. [PubMed: 8087273]

Hemnes AR, Champion HC. Right heart function and haemodynamics in pulmonary hypertension. International Journal of Clinical Practice. 2008; 62:11–19.

Hill MR, Simon MA, Valdez-Jasso D, Zhang W, Champion HC, Sacks MS. Structural and mechanical adaptations of right ventricle free wall myocardium to pressure overload. Annals of biomedical engineering. 2014; 42:2451–2465. [PubMed: 25164124]

Holzapfel GA, Gasser TC. A new constitutive framework for arterial wall mechanics and a comparative study of material models. Journal of Elasticity. 2000; 61:1–48.

Holzapfel GA, Ogden RW. Constitutive modelling of passive myocardium: a structurally based framework for material characterization. Philos Transact A Math Phys Eng Sci. 2009; 367:3445–3475. doi:367/1902/3445 [pii] 10.1098/rsta.2009.0091.

Holzapfel GA, Sommer G, Auer M, Regitnig P, Ogden RW. Layer-specific 3D residual deformations of human aortas with non-atherosclerotic intimal thickening. Annals of biomedical engineering. 2007; 35:530–545. [PubMed: 17285364]

Horowitz A, Lanir Y, Yin FC, Perl M, Sheinman I, Strumpf RK. Structural three-dimensional constitutive law for the passive myocardium. J Biomech Eng. 1988; 110:200–207. [PubMed: 3172739]

Humphrey, JD. Cardiovascular solid mechanics : cells, tissues, and organs. New York: Springer; 2002.

Humphrey JD, Yin FC. On constitutive relations and finite deformations of passive cardiac tissue: I. A pseudostrain-energy function. J Biomech Eng. 1987; 109:298–304. [PubMed: 3695429]

Itskov M, Ehret AE, Mavrilas D. A polyconvex anisotropic strain-energy function for soft collagenous tissues. Biomech Model Mechanobiol. 2006; 5:17–26. [PubMed: 16362195]

Kassab, GS., Sacks, MS. Structure-Based Mechanics of Tissues and Organs. Springer; 2016.

Kenedi, RM.Gibson, T., Daly, CH., editors. Bioengineering studies of human skin. Oxford: Pergamon Press; 1965. Biomechanics and Related Bio-Engineering Topics.

Kodama M, Takimoto Y. Influence of 5-hydroxytryptamine and the effect of a new serotonin receptor antagonist (sarpogrelate) on detrusor smooth muscle of streptozotocin-induced diabetes mellitus in the rat. Int J Urol. 2000; 7:231–235. [PubMed: 10843455]

Lanir Y. A Structural Theory for the Homogeneous Biaxial Stress-Strain Relationships in Flat Collageneous Tissues. J Biomech. 1979; 12:423–436. [PubMed: 457696]

Lanir Y. Constitutive equations for fibrous connective tissues. J Biomech. 1983a; 16:1–12. [PubMed: 6833305]

Lanir Y. Constitutive equations for the lung tissue. J Biomech Eng. 1983b; 105:374–380. [PubMed: 6645447]

Lanir Y. Plausibility of Structural Constitutive-Equations for Isotropic Soft-Tissues in Finite Static Deformations. J Appl Mech-T Asme. 1994; 61:695–702.

Lee C-H, Zhang W, Liao J, Carruthers Christopher A, Sacks Jacob I, Sacks Michael S. On the Presence of Affine Fibril and Fiber Kinematics in the Mitral Valve Anterior Leaflet. Biophysical Journal. 2015; 108:2074–2087. doi:http://dx.doi.org/10.1016/j.bpj.2015.03.019. [PubMed: 25902446]

Macchiarelli G, Ohtani O, Nottola SA, Stallone T, Camboni A, Prado IM, Motta PM. A micro-anatomical model of the distribution of myocardial endomysial collagen. Histology and histopathology. 2002; 17:699–706. [PubMed: 12168777]

Millington P, Gibson T, Evans J, Barbenel J. Structural and mechanical aspects of connective tissue. Adv Biomed Eng. 1971; 1:189–248.

Ogden, R. Nonlinear elasticity, anisotropy, material stability, and residual stresses in soft tissue. In: Ogden, R., editor. Biomechanics of soft tissue in cardiovascular system. New York: Springer; 2003.

Sacks MS. Incorporation of experimentally-derived fiber orientation into a structural constitutive model for planar collagenous tissues. J Biomech Eng. 2003; 125:280–287. [PubMed: 12751291]

Sacks MS, Chuong CJ. Biaxial Mechanical Properties of Passive Right Ventricular Free Wall Myocardium. Journal of Biomechanical Engineering. 1992; 115:202–205.

Sacks MS, Chuong CJ. A constitutive relation for passive right-ventricular free wall myocardium. Journal of Biomechanics. 1993; 26:1341–1345. [PubMed: 8262995]

Sacks MS, Zhang W, Wognum S. A novel fibre-ensemble level constitutive model for exogenous crosslinked collagenous tissues. Interface Focus. 2016; 6

Schmid H, Nash MP, Young AA, Hunter PJ. Myocardial material parameter estimation-a comparative study for simple shear. Journal of Biomechanical Engineering. 2006; 128:742–750. [PubMed: 16995761]

Schmid H, Wang YK, Ashton J, Ehret AE, Krittian SB, Nash MP, Hunter PJ. Myocardial material parameter estimation: a comparison of invariant based orthotropic constitutive equations Comput Methods. Biomech Biomed Engin. 2009; 12:283–295.

Simon MA. Right ventricular adaptation to pressure overload. Curr Opin Crit Care. 2010; 16:237–243. [PubMed: 20179591]

Spencer, AJM. Continuum theory of the mechanics of fibre-reinforced composites. Vol. 282. Springer; 1984.

Stone, AC., Klinger, JR. Pulmonary Hypertension. Springer; 2008. The right ventricle in pulmonary hypertension; p. 93-125.

Streeter, DD. Gross Morphology and Fiber Geometery of the Heart. In: Berne, RM.Sperelakis, N., Geigert, SR., editors. Handbook of Physiology. Baltimore: Williams and Wilkins; 1979. p. 61-112.

Streeter DD Jr, Spotnitz HM, Patel DP, Ross J Jr, Sonnenblick EH. Fiber orientation in the canine left ventricle during diastole and systole. Circulation research. 1969; 24:339–347. [PubMed: 5766515]

Valdez-Jasso D, Simon MA, Champion HC, Sacks MS. A murine experimental model for the mechanical behaviour of viable right-ventricular myocardium. The Journal of Physiology. 2012; 590:4571–4584. [PubMed: 22848044]

Vigano A, Donaldson N, Higginson IJ, Bruera E, Mahmud S, Suarez-Almazor M. Quality of life and survival prediction in terminal cancer patients: a multicenter study. Cancer. 2004; 101:1090–1098. [PubMed: 15329920]

Voelkel NF, Natarajan R, Drake JI, Bogaard HJ. Right ventricle in pulmonary hypertension. Comprehensive Physiology. 2011; 1:525–540. [PubMed: 23737184]

Yin FC, Strumpf RK, Chew PH, Zeger SL. Quantification of the mechanical properties of noncontracting canine myocardium under simultaneous biaxial loading. J Biomech. 1987; 20:577–589. [PubMed: 3611134]

Zhang W, Ayoub S, Liao J, Sacks MS. A meso-scale layer-specific structural constitutive model of the mitral heart valve leaflets. Acta Biomater. 2015

Zhang W, Ayoub S, Liao J, Sacks MS. A meso-scale layer-specific structural constitutive model of the mitral heart valve leaflets. Acta Biomater. 2016; 32:238–255. [PubMed: 26712602]

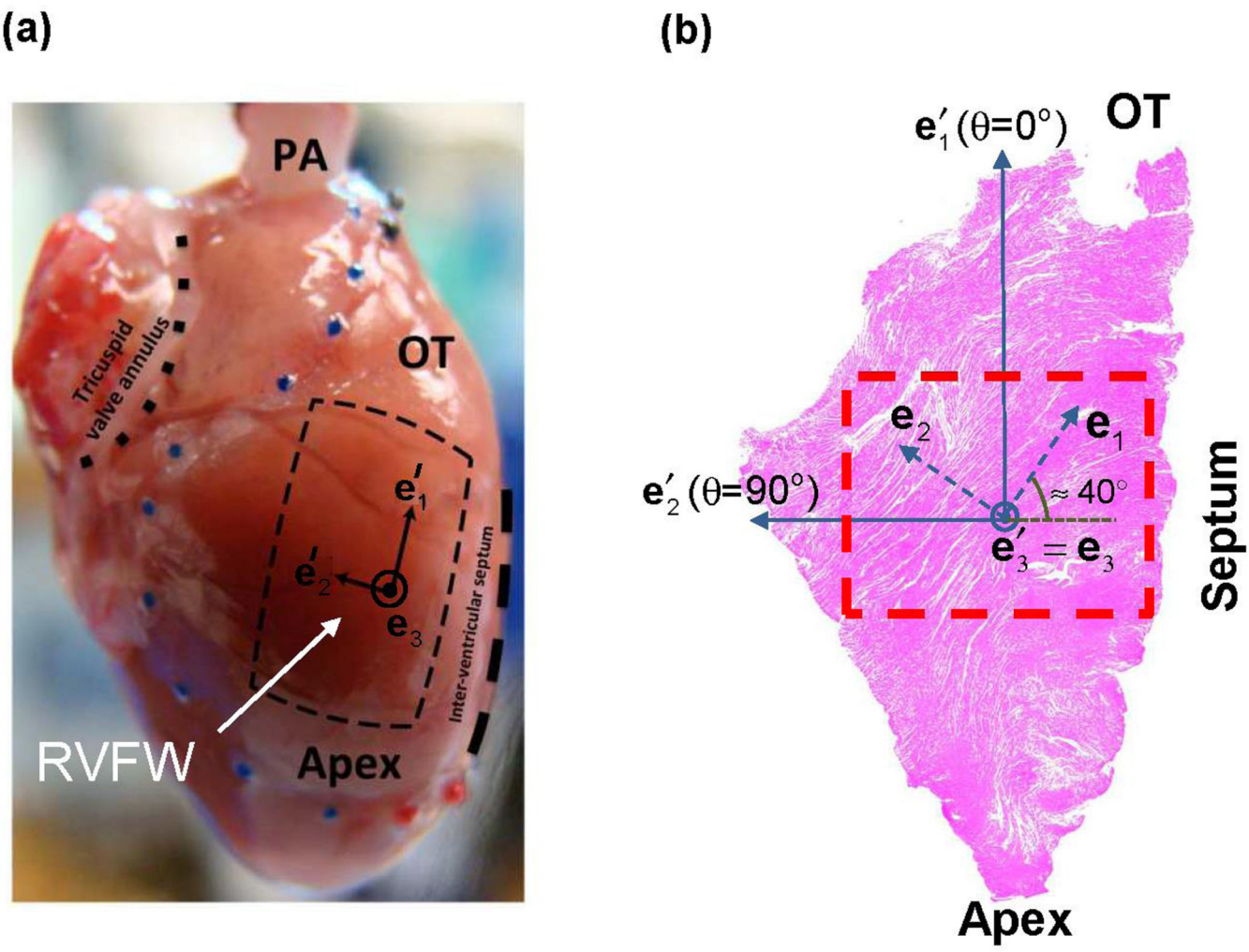

Figure 1.

(a) Isolated rat heart and right ventricular free wall (RVFW), showing outline of RVFW (blue dots) and square slab excised for histological measurements (dashed lines). (b) An example of Gomori-stained histological section used to quantify fiber orientation angle (pink indicates myofibers.) The histological study was limited within the dashed squared box. The mechanical and histological data were measured in the rectangular Cartesian basis $\{\mathbf{e}_1,\mathbf{e}_2,\mathbf{e}_3\}$ and $\{\mathbf{e}_1', \mathbf{e}_2', \mathbf{e}_3'\}$, respectively. The directions $\mathbf{e}_1'$ and $\mathbf{e}_3=\mathbf{e}_3'$ are parallel to inter-ventricular septum and normal to the wall, respectively. The directions $\mathbf{e}_1$ and $\mathbf{e}_2$ are approximately aligned with mean fiber and cross-fiber directions, respectively.

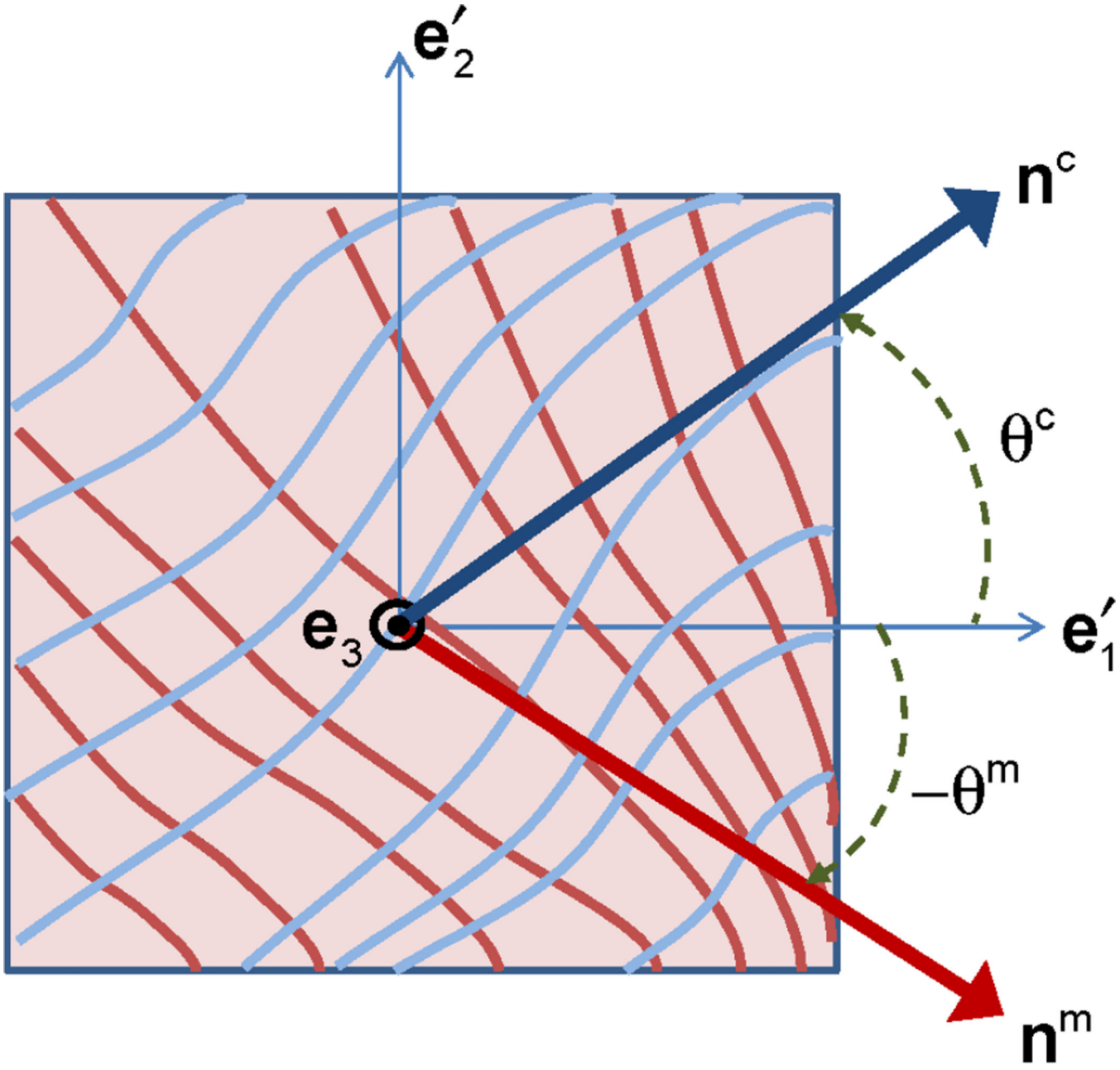

Figure 2.

A schematic illustration of an ensemble of myo- and collagen fibers with uniform (planar) orientations, characterized by unit vectors $\mathbf{n}^{m}$ and $\mathbf{n}^{c}$, respectively.

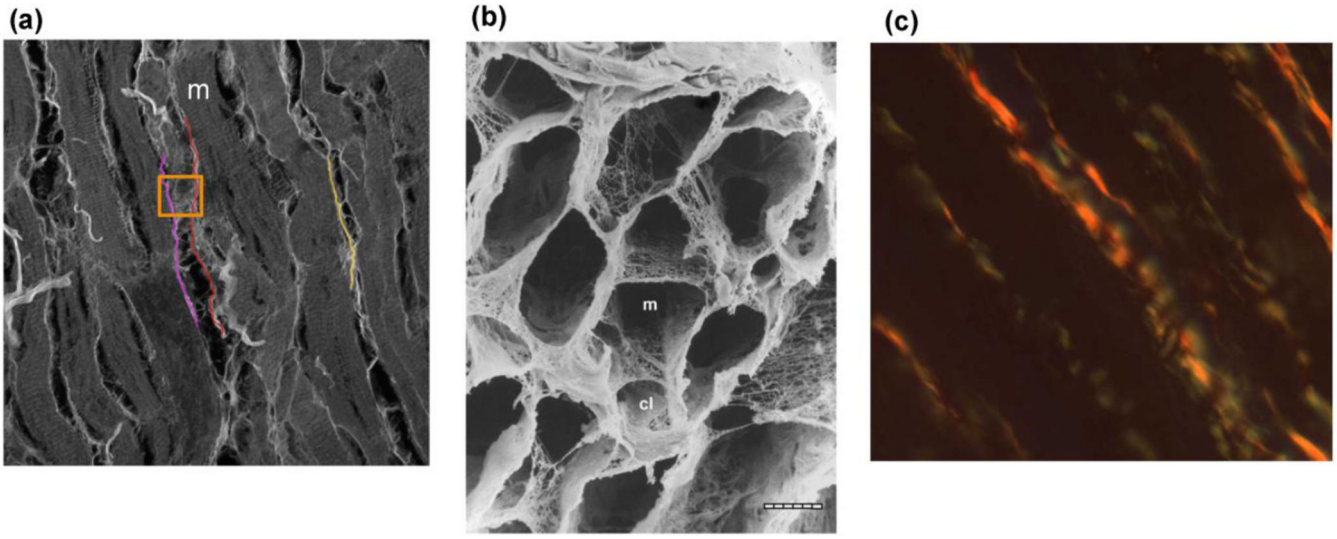

Figure 3.

Microscopic images of myocardium. (a) Numerous myofibers (m) and large collagen fibers (colored strands). Note the presence of a dense network of fine collagen fibers (within orange box). Confocal image. (b) Mesh-like arrangement of fine collagen fiber network (m: myfiber lacunae, cl: capillary lacunae). SEM. Bar = 10 μm. From Macchiarelli (2002). (c) Polarized collagen demonstrating undulated structure. Polarized image of picrosirius red stained myocardium.

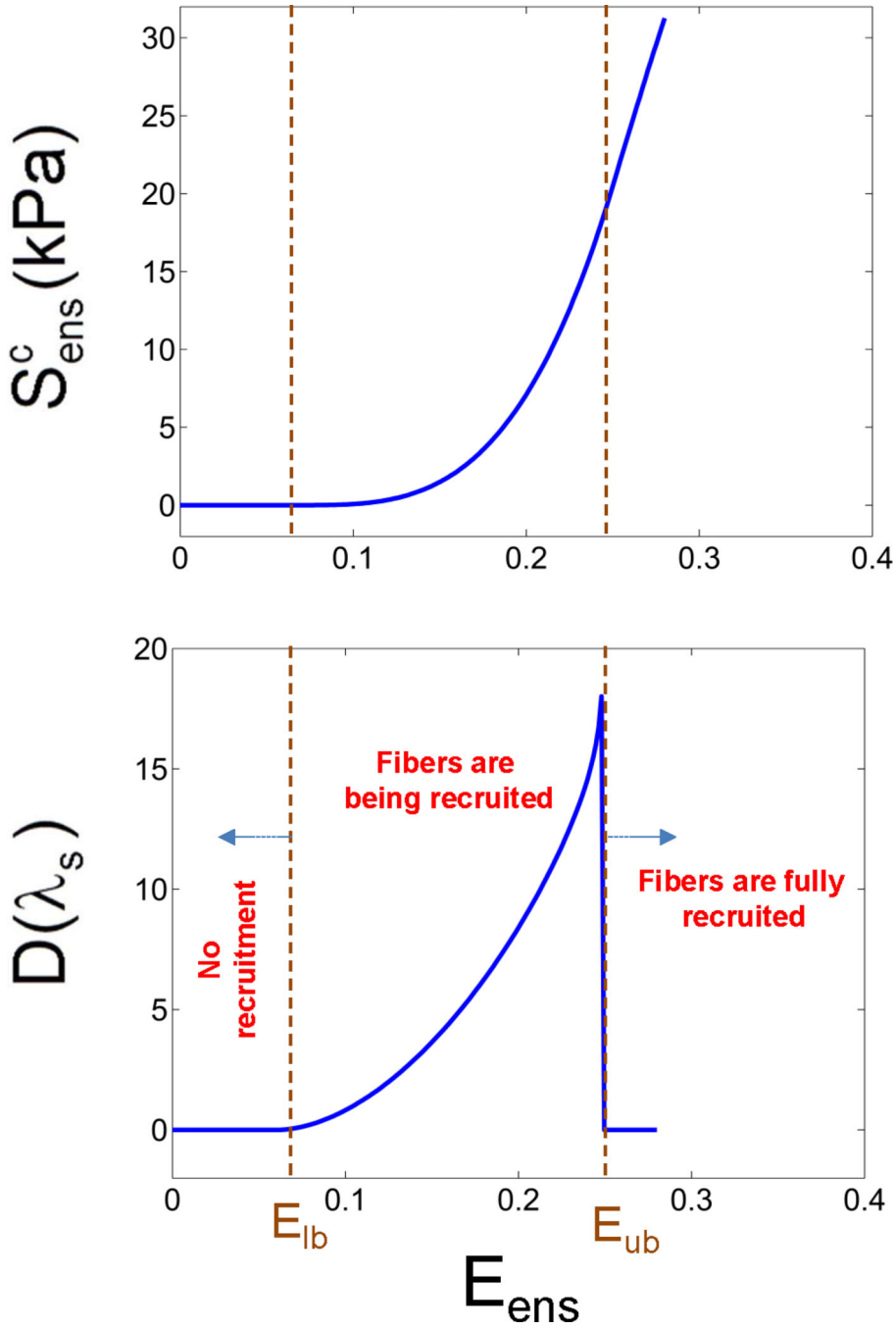

Figure 4.

An example of the collagen fiber ensemble response under equibiaxial loading condition ($E_{ens} = E_{11} = E_{22}$, $S^c_{ens} = S^c_{11} + S^c_{22}$.), and the associated recruitment function.

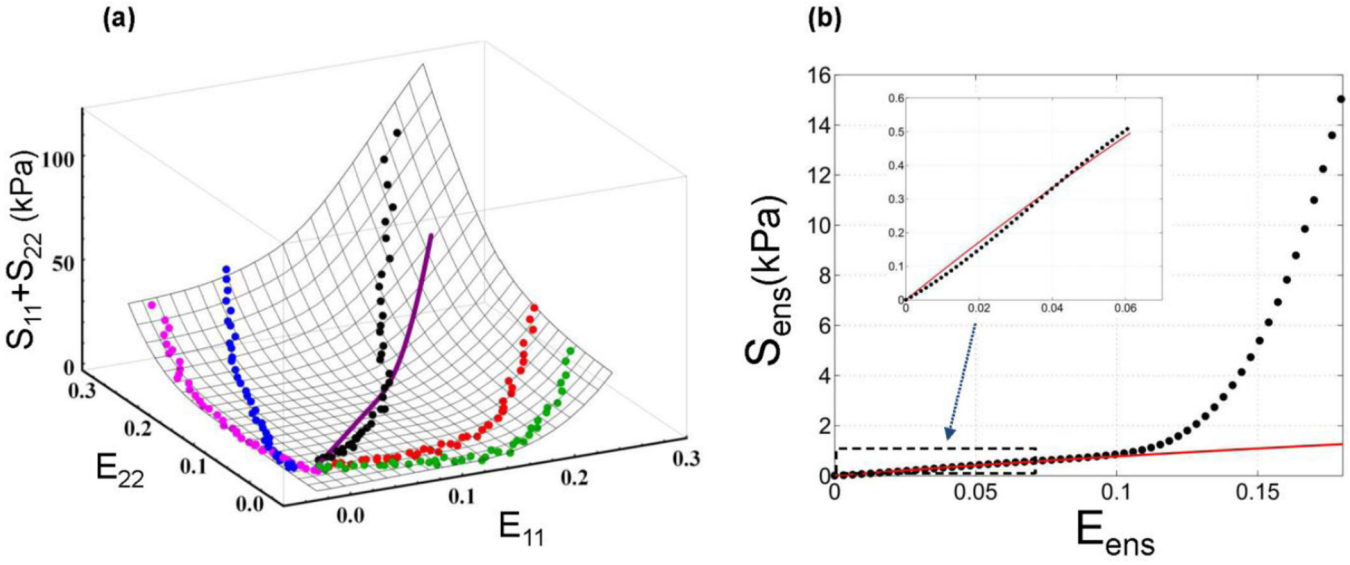

Figure 5.

(a) A representative example of the bicubic Hermite surface that allows us to interpolate the stress values for the equibiaxial loading path (solid line) from other biaxial protocols (markers). (b) A representative example of fitting the myofiber response to the interpolated tissue response in low strain regime under equibiaxial loading condition ($E_{ens} = E_{11} = E_{22}$, $S_{ens} = S_{11} + S_{22}$.)

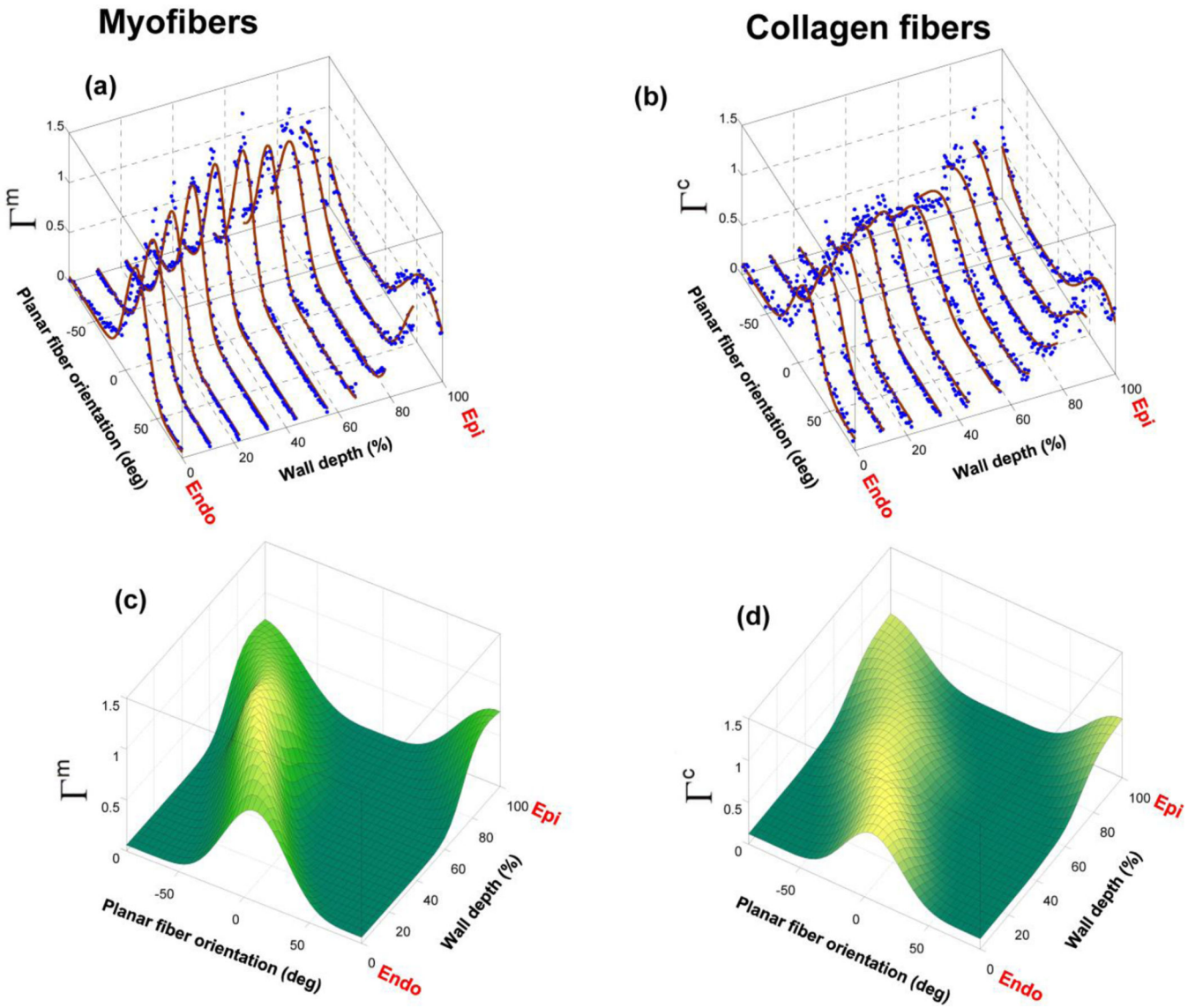

Figure 6.

3D distribution of fiber orientation in RVFW. (a, b) Quantified (planar) orientation distribution for myo- and collagen together with the Beta-distribution fit fiber at ten transmural sections. (c, d) Average surface fit to transmural distributions of myo- and collagen fibers.

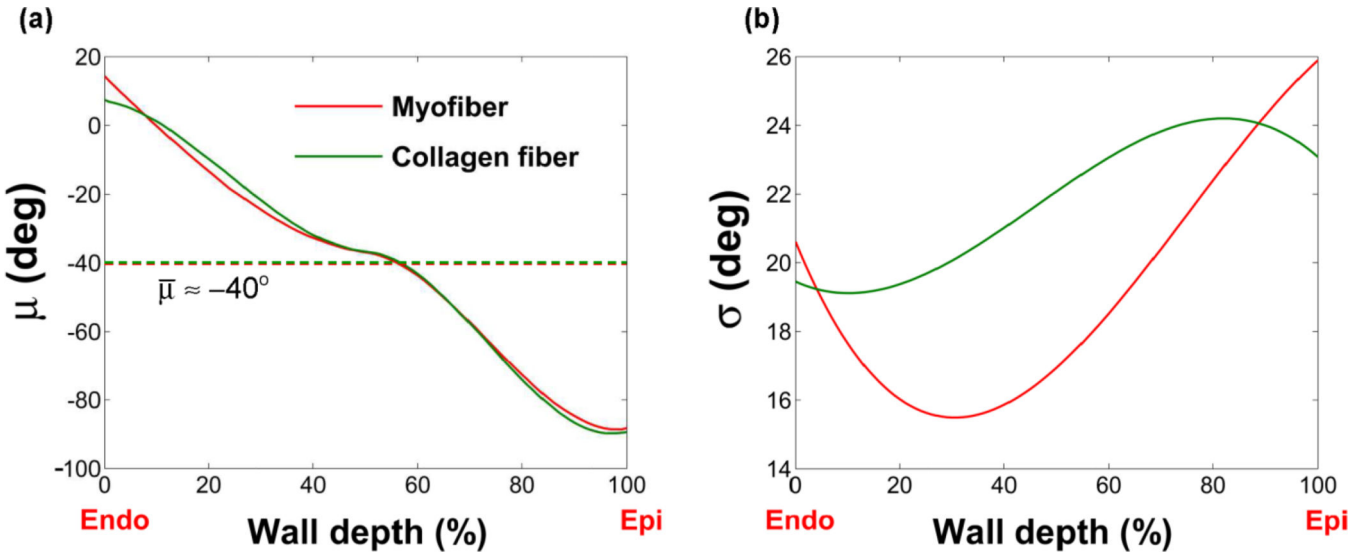

Figure 7.

Statistical measurements of the fitted transmural distribution for myo- and collagen fibers as functions of the wall depth. (a) Mean. (b) Standard deviation.

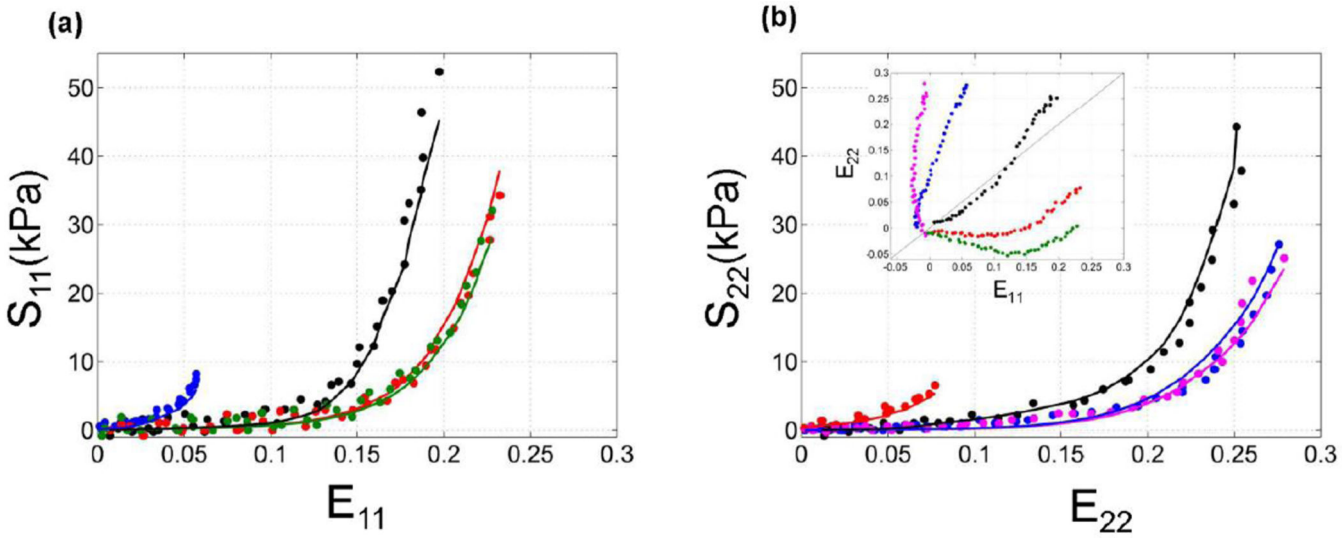

Figure 8.

A representative fit of our constitutive model to the RVFW response (Specimen No. 1). (a) Results for S_{11} as functions of E_{11}. (b) Results for S_{22} as functions of E_{22}. Corresponding biaxial strain protocols are included in Part (b). The stress and strain components are given relative to the basis $\{\mathbf{e}_i\}$ shown in Fig. 1.

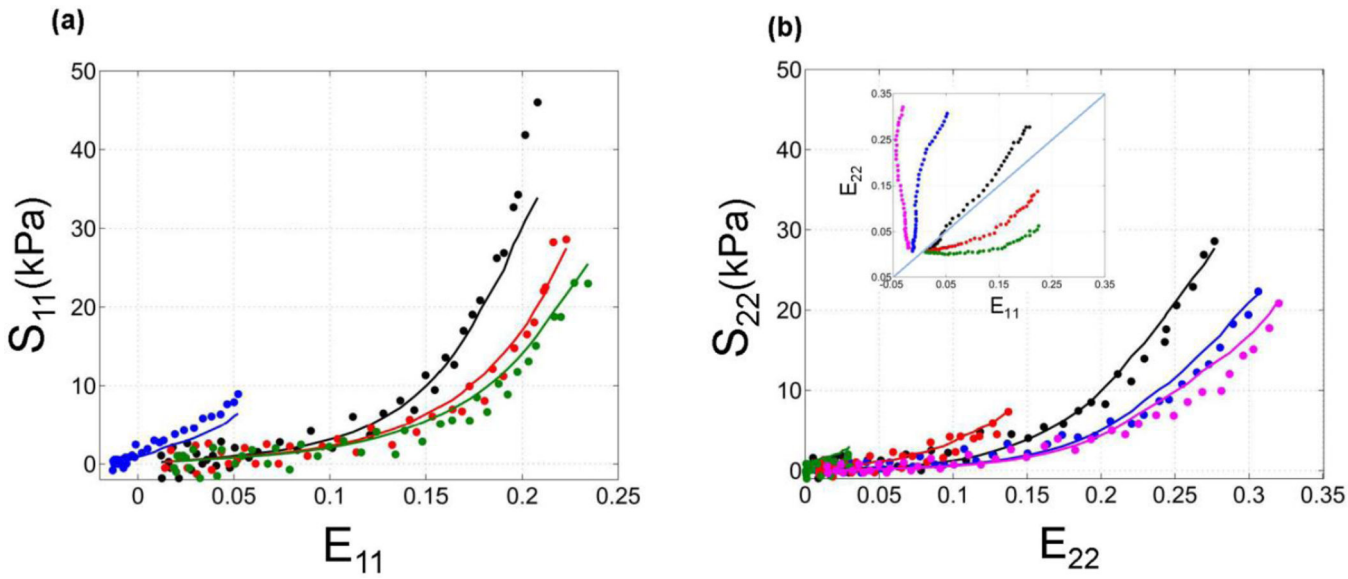

Figure 9.

Predictions of our constitutive model (quantified only through the interpolated equibiaxial response) for the RVFW response under non-equibiaxial loading protocols (Specimen No. 2). (a) Results for S_{11} as functions of E_{11}. (b) Results for S_{22} as functions of E_{22}. Corresponding biaxial strain protocols are included in Part (b).

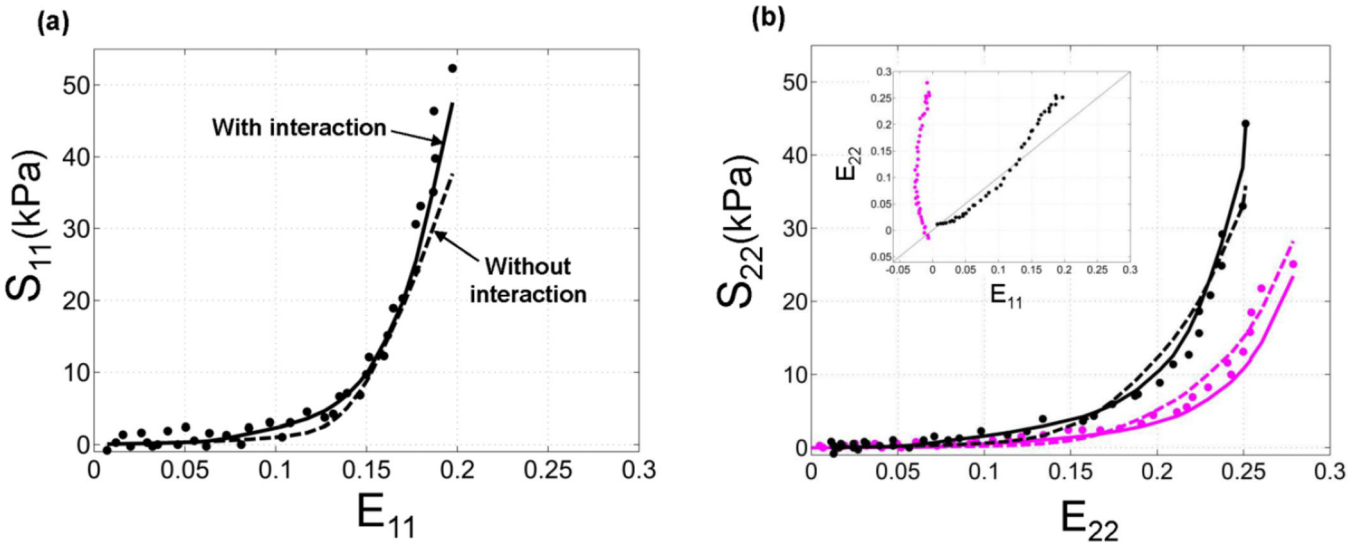

Figure 10.

The effect of including the interaction term in the constitutive model (7) under (nearly) equibiaxial and non-equibiaxial loading conditions. (a) Results for S_{11} as functions of E_{11}. (b) Results for S_{22} as functions of E_{22}.

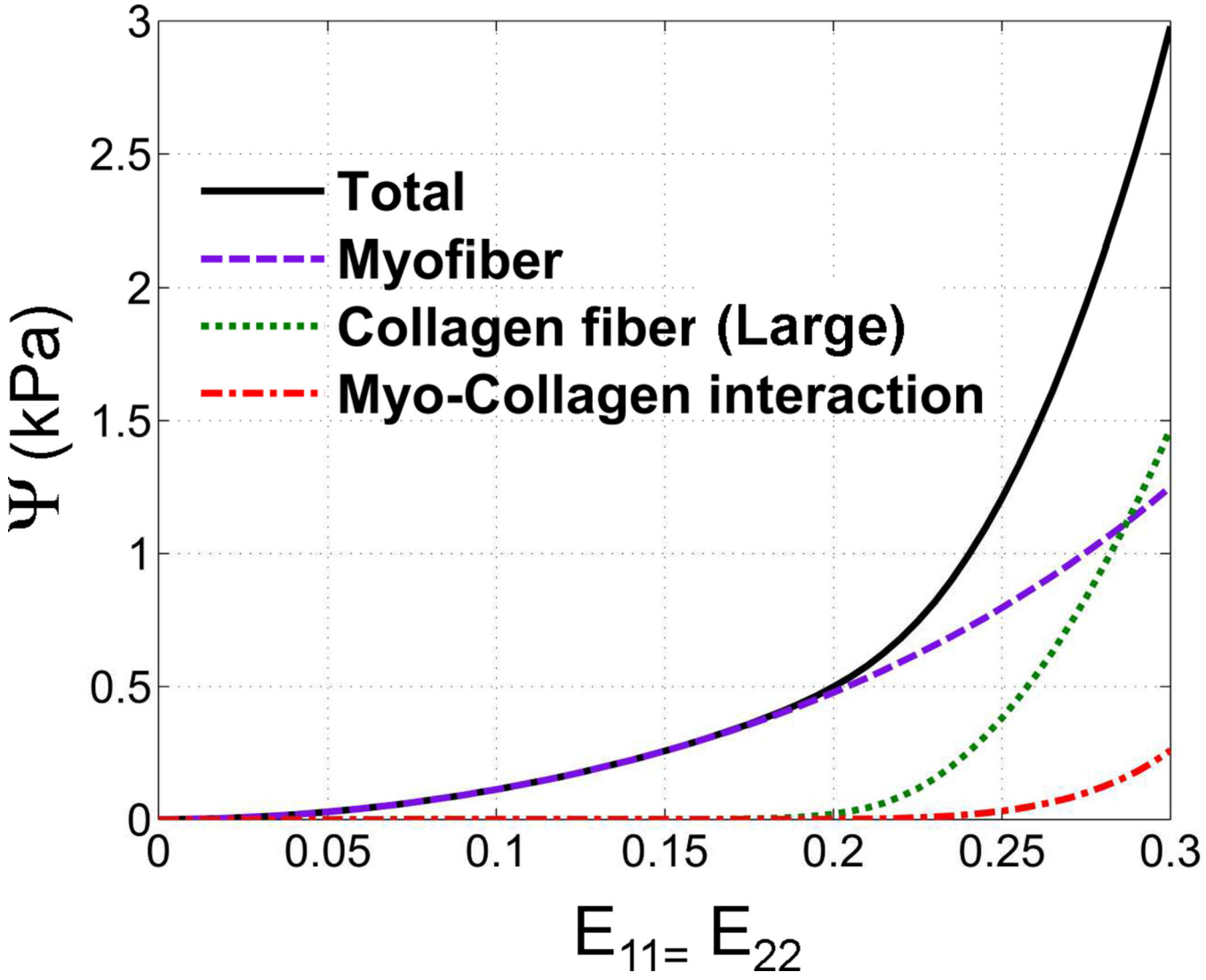

Figure 11.

Prediction of our model for contributions of myo- and collagen fibers and interaction among them in the total energy density as function of applied strain under Equibiaxial loading path. Note that each contributions includes the respective volume fraction term as defined in relation (6). The results correspond to the estimated values of Specimen No. 3 in Table 1.

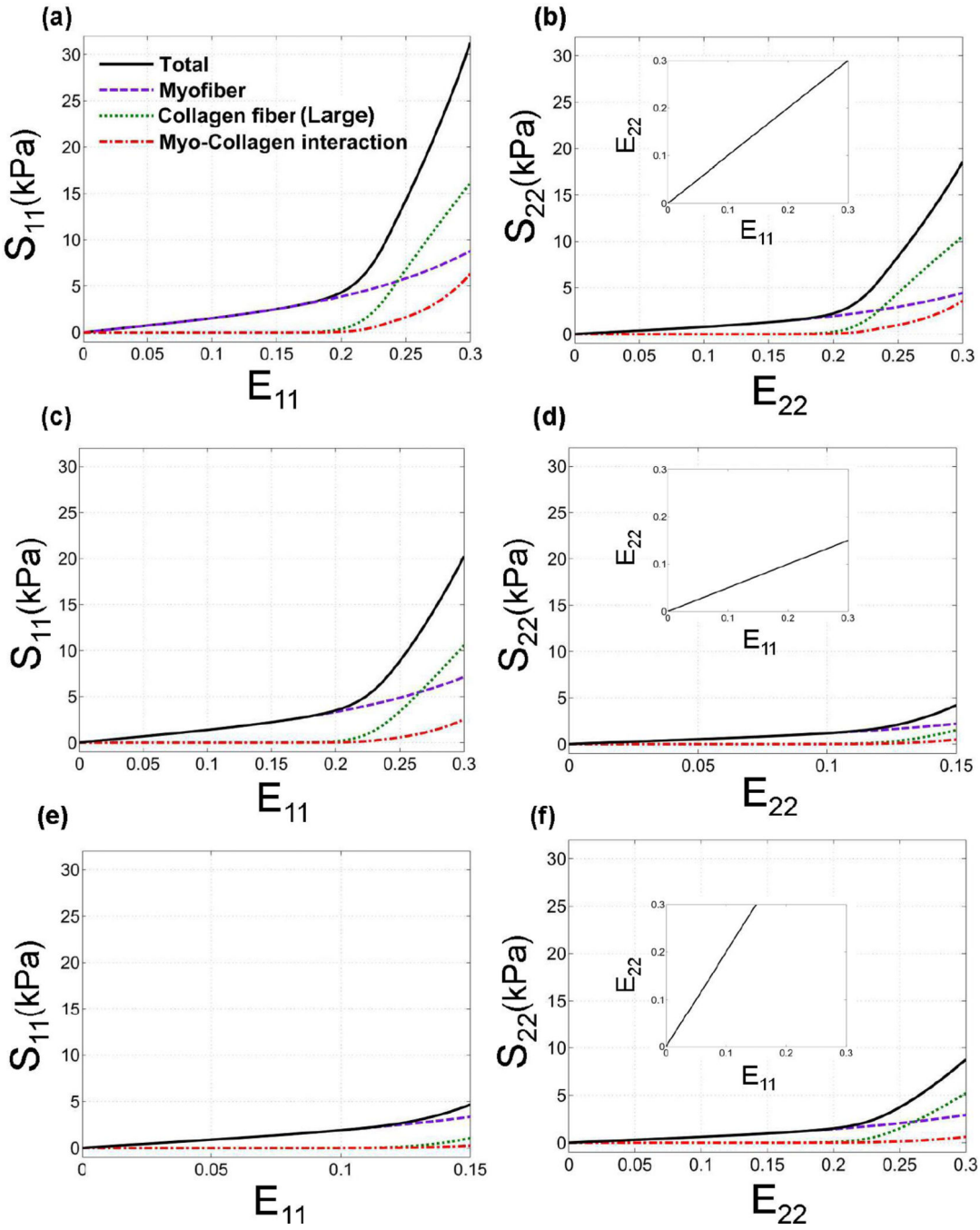

Figure 12.

Predictions of our model for contributions of myo- and collagen fibers and interaction among them in the total stress as functions of applied strain. The results correspond to Specimen No. 3 in Table 1. (a, b) Equibiaxial loading path. (c, d) Loading path $E_{11} = 2E_{22}$. (e, f) Loading path $E_{22} = 0.5E_{11}$.

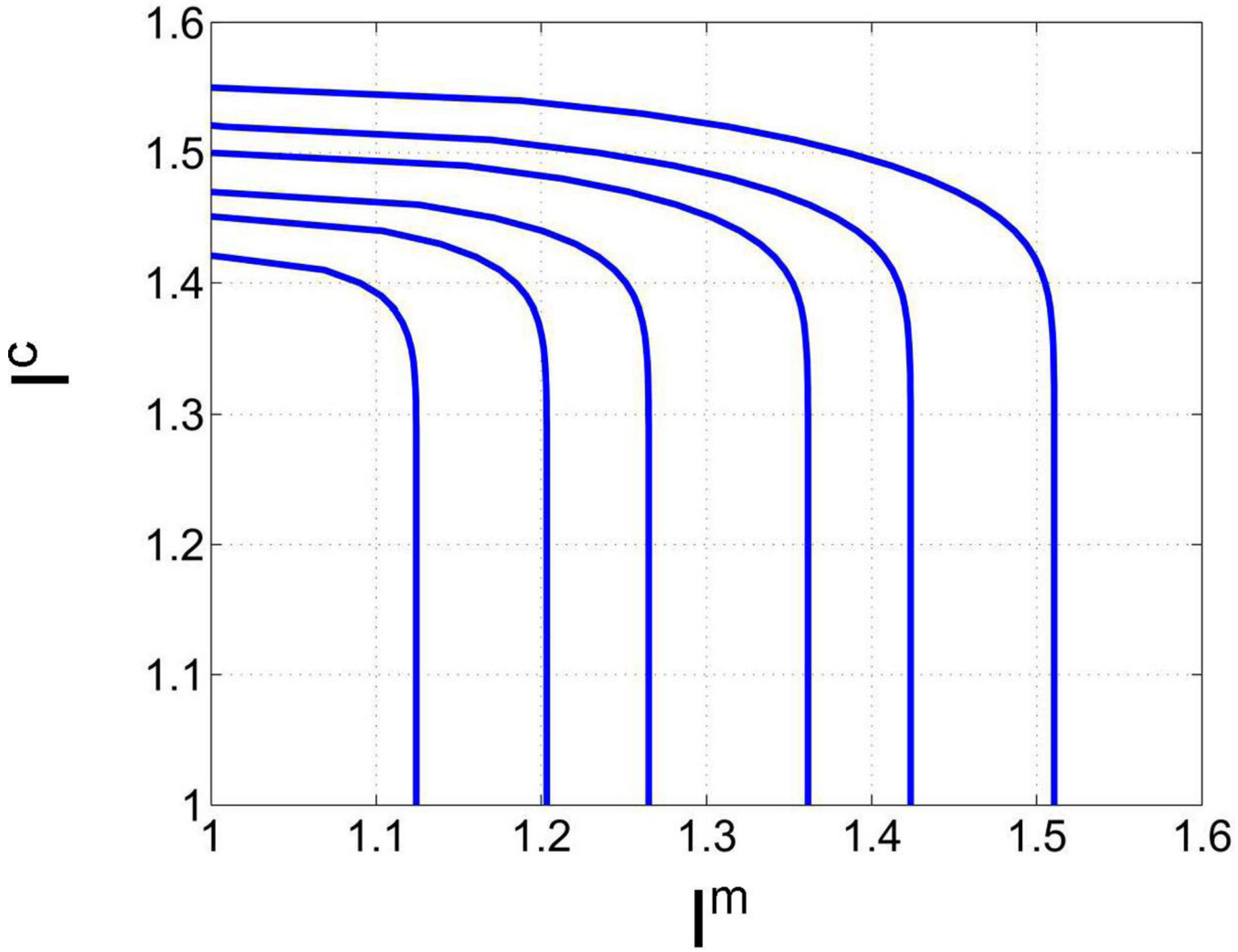

Figure 13.

Contour plots of total potential $\Psi_{\text{ens}}^{\text{Aniso}}(\mathrm{I}^{\mathrm{m}}, \mathrm{I}^{\mathrm{c}})$ for material parameters of Specimen No. 3.

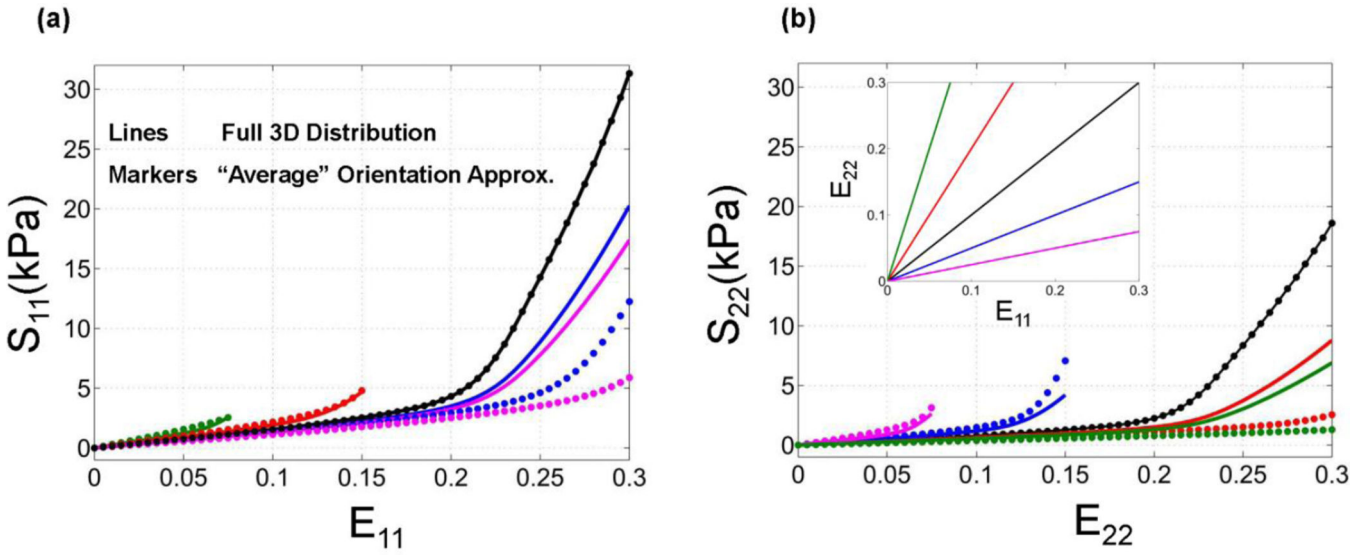

Figure 14.

Comparisons between the results of our model (incorporating transmural fiber orientation distributions) for stress-strain behavior of the RVFW with the corresponding results based on "average" fiber orientation. The results correspond to the estimated values of Specimen No. 3 in Table 1.

Table 1

List of model parameters for five specimens. Except the parameters k_1^m and E_{lb}, the rest of parameters are determined from the fit to all biaxial protocols for each specimen.

	Myofibers		(Perimysial) collagen fibers					Myo-collagen interaction		
				Recruitment						
Specimen No.	k_1^m **(kPa)**	k_2^m	k^c **(MPa)**	E_{lb}	E_{ub}	μ_r	σ_r	k_1^{mc} **(kPa)**	k_2^{mc}	r^2
1	12.80	70.76	3.91	0.061	0.195	0.163	0.030	2.85	7.70	0.97
2	41.22	32.04	4.39	0.039	0.195	0.165	0.030	0.34	3.50	0.96
3	33.91	11.25	2.66	0.052	0.231	0.205	0.016	0.72	6.00	0.95
4	37.33	8.52	1.71	0.061	0.220	0.197	0.016	0.62	6.72	0.94
5	35.38	23.35	6.13	0.049	0.223	0.189	0.027	1.72	6.33	0.93

Table 2

Representative correlation coefficients between selected parameters.

	k_1^m	k_2^m	k^c	k_1^{mc}	k_2^{mc}
k_1^m	1	−0.77	0.30	0.05	−0.04
k_2^m		1	−0.44	−0.1	0.09
k^c			1	−0.33	0.30
k_1^{mc}				1	−0.99
k_2^{mc}					1